Steam-air blown bubbling fluidized bed biomass gasification (BFBBG): Multi-scale models and experimental validation

Richard B. Bates[1], Whitney S. Jablonski[2],Daniel L. Carpenter[3], Christos Altantzis[1,4]Aaron Garg[5], John L. Barton[5], Ran Chen[5], Randall P. Field[6], and Ahmed F. Ghoniem[1]*

1 Department of Mechanical Engineering, Massachusetts Institute of Technology, 77 Mass. Ave. Cambridge, MA 02139, USA
2 National Bioenergy Center, National Renewable Energy Laboratory, 15013 Denver West Parkway Golden, CO, 80401 USA
3 Thermochemical Process Analysis, National Renewable Energy Laboratory, 15013 Denver West Parkway Golden CO 80401, USA
4 National Energy Technology Laboratory, 3610 Collins Ferry Road, Morgantown, WV 26507, USA 15013 5
5 Department of Chemical Engineering, Massachusetts Institute of Technology, 77 Mass. Ave. Cambridge, MA 02139, USA
6 MIT Energy Initiative, Massachusetts Institute of Technology, 77 Mass. Ave. Cambridge, MA 02139, USA

*Richard B. Bates
Address: Room 3-339 77 Massachusetts Avenue Cambridge, MA 02139 USA
Email: rbates@mit.edu
Telephone: +1 617 253 5365
Fax: +1 615-253-5981

Best Paper[1]

Abstract

During fluidized bed biomass gasification, complex gas-solid mixing patterns and numerous chemical and physical phenomena, make identification of optimal operating conditions challenging. In this work, a parametric experimental campaign was carried out alongside the development of a coupled reactor network model (CRNM) which successfully integrates the

[1]This contribution was identified by Michael Molnar (Hemlock Semiconductor Group) as the Best Presentation in the session "Fluidization and Fluid-Particle Systems for Energy and Environmental Applications" of the 2015 AIChE Annual Meeting in Salt Lake City.

individually validated sub-models to predict steady-state reactor performance metrics and outputs. The experiments utilized an integrated gasification system consisting of an externally-heated, bench-scale, 4-inch, 5kWth, fluidized bed steam/air blown gasifier fed with woody biomass equipped with a molecular beam mass spectrometer (MBMS) to directly measure tar species. The operating temperature (750-850 $^{\circ}$C) and air/fuel equivalence ratio (ER=0-0.157) were independently varied in order to isolate their effects. Elevating temperature is shown to improve the char gasification rate and reduce tar concentrations. Air strongly impacts the composition of tar, accelerating the conversion of lighter polycyclic-aromatic hydrocarbons into soot precursors, while also improving the overall carbon conversion.

1. **Introduction**

Concerns over climate change as an urgent threat to the existence of human society, have spurred the successful negotiation and drafting of an unprecedented global agreement[1]. In order to avoid potentially irreversible damage to the planet, nations have agreed to progressively ambitious emission goals. While a variety of technologies will certainly be required to achieve these targets, the development of alternatives to traditional fossil-based transportation fuels is crucial. Lignocellulosic biomass is a greenhouse gas (GHG) neutral feedstock which- although highly diffuse and variable- is relatively abundant at competitive costs. According to the US Department of Energy (DOE) and Agriculture (USDA), if the one billion tons of potential and available woody and herbaceous feedstocks were converted to fuels they could annually displace approximately 30% of domestic petroleum usage [2,3].

The thermochemical pathways to convert biomass to liquid fuels can be categorized by the severity of the temperature application. The gasification route, where biomass is partially oxidized at high temperatures (greater than 700°C) to produce syngas (a mixture of carbon monoxide and hydrogen), is particularly promising due to the long history of industrial practice with coal[4] and other gaseous and liquid[5] hydrocarbon feedstocks. However, biomass poses unique gasification challenges due to its variable nature, high moisture content, alkali/alkaline earth metal content, and expense in size-reduction. As a result, fluidized bed reactors, with their favorable heat transfer characteristics, offer promising benefits and have been employed in a number of single, dual [6] and multi stage configurations[7] to process a variety of feedstocks. While multiple configurations have been proposed, they can be further classified as indirect (allothermal) or direct (autothermal). In the former, heat is supplied through heat exchange while

in the latter the direct injection of oxygen liberates the necessary thermal energy to drive the endothermic gasification reactions. In this case, the sub-stoichiometric injection of oxygen, commonly defined by the air-fuel equivalence ratio (ER), is usually limited between 0.2-0.4, with the actual amount determined by the desired operating temperature[8]. ER is defined as the actual amount of oxygen fed to the gasifier divided by the stoichiometric amount of oxygen required for complete combustion of the biomass [9].

Fluidized bed biomass gasification (FBBG) faces three major technical challenges related to the i)production of tars, ii) incomplete conversion of char, and iii) the high methane content, which depending on the end use, must be subsequently reformed[10]. Tars are condensable organic compounds produced in significant quantities (>2g/Nm^3)[11] under most operating conditions, and -unless removed- they cause a variety of downstream operational issues including fouling, plugging, and corrosion. Resistant to thermal treatment, tars require elevated temperatures around 1000–1300°C to decompose into lighter products [12,13]. Char conversion is limited during FBBG because of a number of competing physical and chemical processes including inhibition, attrition, and elutriation[14]. For example, during steam gasification at 850-950°C an upper limit of carbon conversion of 30-70% was observed [15], and demonstration-scale gasifiers have exhibited 50-80% of the fixed carbon in the char being elutriated and unconverted[16–18]. Because of its high thermodynamic stability [19] under non-catalytic operating conditions, methane is present in significant quantities (4-12%vol dry) [20] which constitutes up to 30-40% of the product gas' energy content.

The primary measures to optimize FBBG are either operation or design related. The manipulation of operational parameters such as the temperature[21], pressure[22], in-bed additives [23], steam to biomass ratio (S/B) [17,24], and air/oxygen input (ER) [9] have been widely studied through

experiments. The optimization of FBBG through the experimental study of operational variables has proven difficult because the extremely complex, overlapping physical and chemical phenomena occurring within the reactors obscure the actual causal mechanisms [17]. Increasing the air/oxygen injection, acts to raise the operating temperature, decrease tar production and increase char conversion; however the overall heating value of product gas is reduced, and the risk of agglomeration of the bed material is increased [25]. These competing effects suggest that a "thermally" optimal amount of air/oxygen exists when the product of the heating value and yield of the gas is maximized. That said, it is not well understood how to operate or design direct gasification reactors systems in such a way that the inputted oxygen selects the char and tars instead of the more reactive- but desirable- light gases such as hydrogen and carbon monoxide[16]. For example, there is disagreement as to whether oxygen preferentially reacts with these light gases in a small region near the bottom of the bed [26,27] or if char oxidation dominates the consumption[27]. The methane content appears to be largely unaffected by variations in temperature or oxygen input [26].

A number of researchers have examined the secondary injection of air/oxygen in pilot scale systems as a primary design measure to partially oxidize the tars in the freeboard region of the gasifier [11,28,29]. The total amount of oxygen is kept fixed ($0.2<ER<0.4$) but is split between the distributor and freeboard injection locations. These studies demonstrated a reduction in tar content to as low as 0.4 g/Nm^3 during forest residue gasification; however, the gas lower heating value (LHV) decreased linearly with a greater proportion of secondary injection. Moreover, this is still an order of magnitude higher than the desired product gas tar concentration limits which depend on the end application. Engine and turbine applications require the tar content to be under <0.01g/Nm^3, while synthesis reactors require a concentration <1 ppmv [10,20].

The addition of steam as a gasifying agent also appears to have competing effects because -on the one hand- it lowers the operating temperature of the bed (under adiabatic conditions) while also promoting hydrogen production through the steam gasification and water gas shift reactions [24,25,30]. However, this optimal amount depends on the operating temperature [17], making it difficult to generalize these values.

In-bed additives have demonstrated a significant impact on the product gas composition. Corella et al. compared raw olivine $(Mg,Fe)_2SiO_4$ and dolomite ($CaO \cdot MgO$) and found the latter more effective, resulting in tar contents as low as 1-2 g/Nm[37]. Koppatz et al. found olivine reduced the gravimetrically detected tars in the product gas to 5-7 g/Nm^3 -a 60% reduction compared to using silica sand [31].

The apparent limitations of using primary measures to achieve desired performance metrics has resulted in the proposal and design of a variety of dual or multi-stage systems which can be understood as attempts to isolate the various chemical processes by spatial separation (i.e multiple reactors or zones)[7,25]. Of these, one of the longest studied was proposed by researchers at Vienna University of Technology (VUT) [6] and further developed into a pilot scale ($8MW_{th,fuel}$) combined-heat and power (CHP) system at Güssing, Austria [32]. In these dual stage systems, biomass is gasified with steam in one reactor and the residual char is combusted in a separate vessel[31,33]. Steady circulation of bed material between the endothermic gasification bed and the exothermic combustion reactor is necessary to maintain an overall energy balance; however it is not clear what benefit some distribution air/oxygen between the reactors would have. Schuetzle et al. recently examined the impact of adding minor amounts of air into a multi-stage pilot-scale process which included a pyrolysis retort chamber operating between 760–843°C and a subsequent steam reforming operation at 977-991°C[34]. Increasing the air input resulted in oxygen

concentrations between 0.0225 to 4.1 percent volume as well as a significant increase in the concentration of polycyclic aromatic hydrocarbons (PAH's) and soot (particulate carbon). However, the precise location of air injection during this process was not specified making it difficult to understand the mechanisms through which this occurred. Other multi-stage processes have included a partial oxidation of the product gases [35–37] to mitigate tars; however, questions regarding the efficiency of partial oxidation given the relative reactivity of the desirable light gases and tars remain.

In summary, the fate of oxygen and steam injected into gasification or pyrolysis systems has yet to be definitively answered through existing experimental or modeling efforts. Therefore this work aims to fill the significant gaps through a combined experimental and modeling investigation. First a review of the processes occurring in a fluidized bed a nd state of the art modeling approaches is followed by the development of a multi-scale model. Then the materials and methods for the steam/air blown gasification experiments in a 4 inch fluidized bed reactor (FBR) are described. The results section validates the model predictions against the experimental data, discusses important trends, and identifies operational recommendations.

2. Fluidized bed biomass gasification

2.1. Physical and chemical processes

A number of complex physical and chemical processes occur simultaneously over a range of spatial and time scales during FBBG. These are shown schematically in Figure 1.

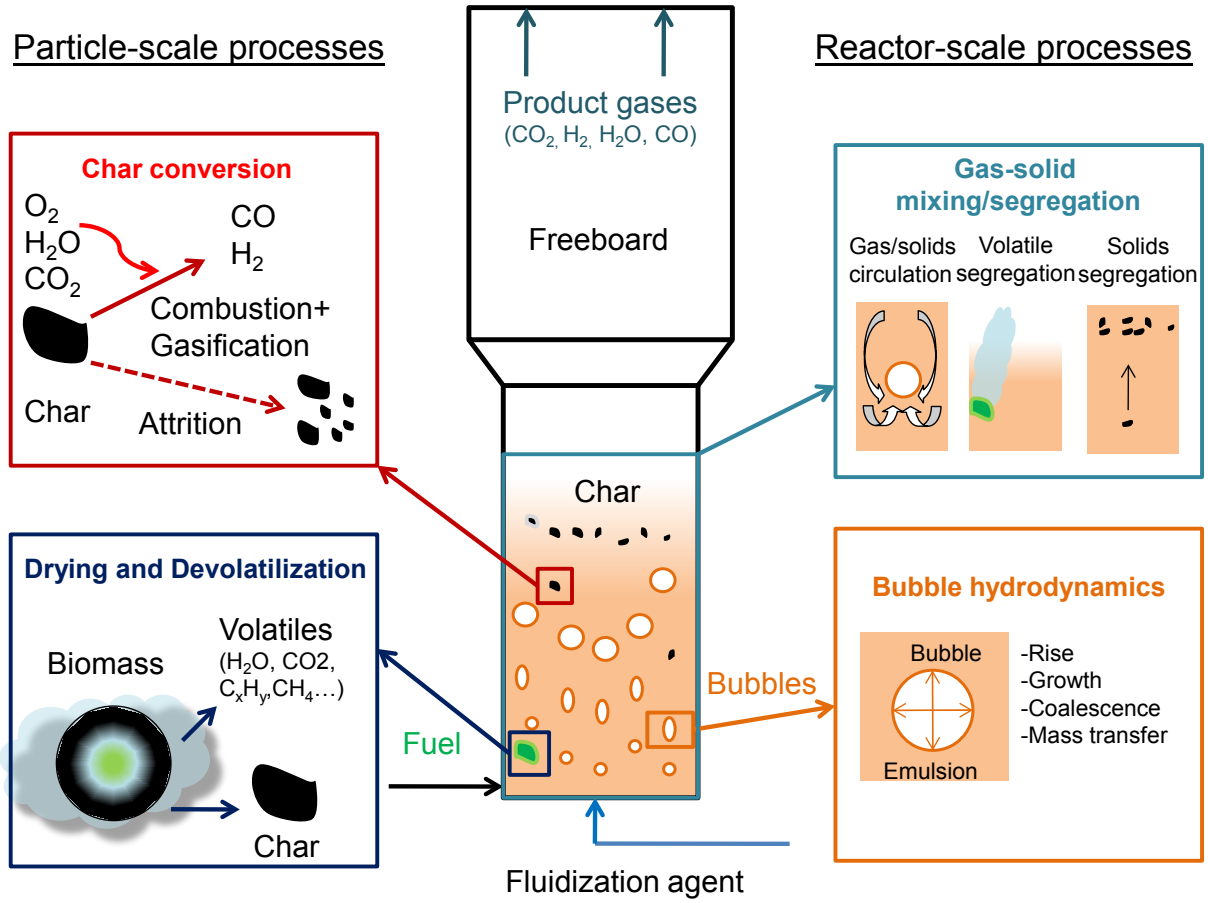

Figure 1 Particle and reactor scale processes occurring during fluidized bed gasification

The unique hydrodynamic behavior of the reactor is caused by the fluidization of a granular material (silica sand, olivine, dolomite etc.). This occurs when a gas (e.g. steam or air) is injected in excess of a minimum fluidizing velocity (u_{mf}) such that the drag force incurred by the flow through the particle interstices becomes equal to their weight minus buoyancy force[38]. In the bubbling fluidization regime, a clear distinction between two 'phases' is apparent: the bubble phase consists of vertically rising regions of high gas (void) volume fraction, and the emulsion phase is composed of densely packed circulating solids. Gas-solid flow patterns within the bed are dominated by the chaotic motion of the bubbles through the emulsion phase[39]. However, under certain conditions, segregation of volatile matter [40] or char [41,42] and agglomeration of solids [43] can adversely affect the flow patterns. During proper fluidization, this circulatory motion combined with the large heat capacity of the bed materials, results in effective heat transfer to the reacting particles. As a result, as soon as biomass particles enter the gasifier they rapidly undergo drying and devolatilization resulting in tars, light gases (e.g. CO_2, CO, H_2,CH_4) and char [44]. The primary pyrolysis vapors are a complex mixture of oxygenated compounds (e.g acetic acid, lactic acid, methanol), anhydrosugars (levoglucosan $C_6H_{10}O_5$, xylofuranose $C_5H_{10}O_5$) and phenolic lignin degradation products. Due to the fast release of volatiles, the reactive gases surrounding the particle are unable to penetrate into the particle and thus the devolatilization occurs in an inert environment and is therefore referred to as pyroylsis [45].

Next, the liberated volatiles form endogenous bubbles and participate in a complex network of homogeneous reactions within the bed and freeboard including oxidation, steam reforming, cracking, and water-gas shift [46]. The ratio of the mass of volatiles to the initial

fluidization agent is usually significant and therefore strongly influences the bed hydrodynamics [47,48].

The subsequent char formed by devolatilization participates in heterogeneous reactions with steam, carbon dioxide, oxygen as well as undergoing physical deterioration due to fragmentation and attrition. The attrited fines are much smaller than the mother char particles and are blown out (elutriated) from the reactor rapidly as unconverted carbon[49].

2.2.Existing modeling efforts

The variety of existing models for FBBG can be categorized by the fidelity with which they describe the bed hydrodynamics[45]. In order of increasing hydrodynamic complexity these include black box models (BBM), fluidization models (FM), and computational fluid dynamic models (CFDM). Black box models, do not resolve the processes occurring with the reactor, and apply generalized balances (e.g heat and mass) around the reactor or to zones within the reactor. Lacking kinetics, they make assumptions regarding chemical equilibrium (or pseudo-equilibrium)[26]. CFDM have the advantage that they fully resolve the hydrodynamics, but due to their computational complexity, are currently limited in the geometric size and time length of simulations. For example, 2D reactive [50] and 3D reactive simulations [51,52] have been limited to lab scale geometries (d_b=40-220mm and L=0.2-1.4 meters) and short times (30-200 seconds). Fluidization models (FM) are reduced order models which avoid the complexity associated with solving momentum transport equations by approximating the reactor hydrodynamics with semi-empirical correlations. Widely adopted in the modeling of coal gasification, they were first applied to biomass gasification by Raman et al. [53]. At least 19 separate FM have been developed

since then making them most commonly applied and advanced models developed for fluidized bed biomass gasification[45].

The major deficiencies in these previous modeling approaches are related to the description of the i) gas phase chemistry and ii) char conversion. The decomposition of biomass constituents (lignin, cellulose, hemicelluloses) is extremely complex and is still an area of current investigation. As a result, the composition of primary pyrolysis vapors has usually been modeled semi-empirically[44]. Secondary gas phase reactions are usually modeled in a lumped manner[54], require tuning parameters [55], or neglected altogether. Recent attempts to describe, secondary tar conversion can be further classified as global or detailed. In the former, apparent reaction rate expressions for individual species of interest are assembled from the literature to generate a single mechanism [56,57]. Recently Fuentes Cano et al., [57] developed a global model considering two representative primary tars, acetol (C_3H_6O2) and catechol ($C_6H_6O_2$) reacting to produce 10 product species with 12 reactions. Detailed mechanisms consist of a much larger number of elementary reactions and species, incurring a significant computational demand. Stark et al. [58] utilized a detailed gas phase kinetic mechanism comprised of 327 species 10933 reactions developed by Ranzi et al. [59] to analyze air-blown fluidized bed gasification. Solving the mechanism in an equivalent reactor network (ERN) model, the impact of gasifier temperature and ER on gravimetric tar destruction were demonstrated; however char combustion and gasification were not considered under those conditions. Recently, a kinetic mechanism for the vapor phase reactions of cellulose (500 species and 8000 reactions) has been assembled and validated experimentally [60] which was later coupled with global mechanism for lignin-derived volatiles [61].

Prediction of char conversion is the most important factor in accurately modeling fluidized bed gasifier performance, yet in almost all previous models, elutriation phenomena of char are neglected or unspecified. As a result, char conversion itself must be assumed to occur completely within the bed *a priori* [62,63]. Modeling reductions in fuel size by fragmentation and attrition are rarely included [40,53,62–68]. The most comprehensive models developed by Souza-Santos [69] and Hamel and Krumm [70] sub-models for fragmentation and attrition and elutriation; however, the predicted flow rates of entrained solids is poor and incorrect by up to several orders of magnitude [69].

2.3. Time scale analysis

Having identified the major phenomena and existing modeling limitations, it is important to judiciously identify simplifying assumptions which may be made in order to develop a computationally tractable yet sufficiently descriptive model. A time scale analysis [14,71] provides a valuable framework with which to judge the sequence, coupling, and relative importance of various phenomena to include. Moreover, the ratios of the time-scales yield important dimensionless numbers which can serve as useful design and scaling criteria.

2.3.1. Particle scale processes

The initial release of volatiles from biomass particles in fluidized beds involves several simultaneous thermal and chemical processes. After a particle is introduced to the reactor, external heat transfer to its surface and within it, leads to high temperature drying (>100°C) and devolatilization at temperatures between 200-800°C [72]. Solids mixing occurs at different rates

depending on whether the direction of the particle motion is lateral (or radial) or axial, with the latter being roughly one order of magnitude greater than the former [73]. An axial solids circulation time or "turnover time" refers to the time taken for a particle to travel to travel the height of the bed and back down [73]. A dispersion coefficient based on the correlation from Borodulya et al. [74] is used to compute a lateral mixing time scale. A power law correlation developed empirically by Gaston et al. [75] can be used to estimate the overall devolatilization time $t_{pyr,eff}$ in a fluidized bed for oak particles between 6mm and 25mm. For consistency in comparison, the physical properties of the biomass, reactor, and bed material, were taken from the same study [75]. Definitions of the characteristic time scales are shown in Table 1.

Table 1 Time scale analysis for particle devolatilization and mixing

Transport process or reaction	Characteristic time scale (sec)	Source
Physico-chemical processes		
Pyrolysis kinetic time scale	$t_{pyr,kin} = 1/3.27 * 10^6 exp(-113900/R_g T)$	Biagini et al., [76]
Internal heat transfer time scale	$t_{int,HX} = \frac{\rho_{bio} c_{p,bio} d_{bio}^2}{36 k_{bio}}$	
External heat transfer time scale	$t_{ext,HX} = \frac{\rho_{bio} c_{p,bio} d_{bio}}{6 h_{avg}}$	
Pyrolysis effective time scale	$t_{pyr,eff} = 1.746 * 10^4 \, exp(1013.2/T^{1.076}) \, {d_{bio}}^{1.414}$	Gaston et al. [75]
Drying time scale	$t_{dry} = 1/4.5 * 10^3 \, exp(-45000/\mathrm{RT})$	Parker et al. [78]
Hydrodynamic processes		
Solids mixing time scale	$t_{mix,axial} = H_{bed}/0.6(u_0 - u_{mf})$	[79]
Lateral mixing time scale	$t_{mix,lateral} = d_{bed}^2/(2\, D_L)$ $D_L = 0.013(u_0 - u_{mf}) H_{mf} (d_{bed}/H_{mf})^{0.5} (Fr)^{-0.15}$ $Fr = (u_0 - u_{mf})^2/(g H_{mf})$	[80] [74]
Physical properties and correlations		
Apparent biomass density *Biomass effective thermal conductivity* *Biomass specific heat capacity*	ρ_{bio}=820 kg/m^3 (oak) $k_{bio} = 0.285$ W/mK (oak) $c_{p,bio} = 1800$ J/kg-K	[81] [82] [72]
Bed mass, particle size, density *Superficial, minimum fluidization velocity* *Bed diameter, static bed height* *Reactor temperature, pressure*	m_{bed}=3kg d_p=270μm ρ_p=3300 kg/m^3 (olivine) u_0~ 0.115 $u_{mf} = 0.033$ (m/s) $d_{bed} = 0.104$ m $H_s = 0.186$ m T= 1073K P=101325 Pa	Current study
Solid-solid Nusselt number (d_{bio}>>d_s) *Gas-solid Nusselt number* *Effective heat transfer coefficient* *Archimedes number* *Reynolds number* *Prandtl number*	$Nu_s = 0.85 {Ar_s}^{0.19} + 0.006 Ar_s^{0.5} Pr^{1/3}$ $Nu_f = 2 + 0.6(Re_{mf}/\varepsilon_{mf})^{0.5} Pr^{1/3}$ $h_{avg} = (Nu_s k_f/d_p + Nu_f k_f/d_{bio})/2$ $Ar_s = \rho_f(\rho_s - \rho_f) g {d_s}^3/{\mu_f}^2$ $Re_{mf} = \rho_f u_{mf} d_{bio}/\mu_f$ $Pr = \mu_f c_{p,f}/k_f$	[45,83] [72] [72]

The characteristic time scales versus the biomass particle diameter are shown in Figure 2. The characteristic length used in the analysis is the volume/surface mean diameter in meters[14]. Several important conclusions can be drawn from this analysis. For millimeter-scale particles, heat transfer processes are the dominant resistance to particle conversion and take much longer than pyrolysis or drying kinetics (evaluated at 800°C). These heat transfer limitations cause the particles to experience a time-varying temperature profile during these chemical processes. The ratio of the internal and external heat transfer time-scales ($t_{int,HX}/t_{ext,HX}$) gives the thermal Biot number which is approximately one for 6mm particles and decreases with decreasing particle size. When d_{bio}<0.5mm, then Bi<0.1 meaning that the particles can be rigorously assumed as uniform in temperature during their heating.

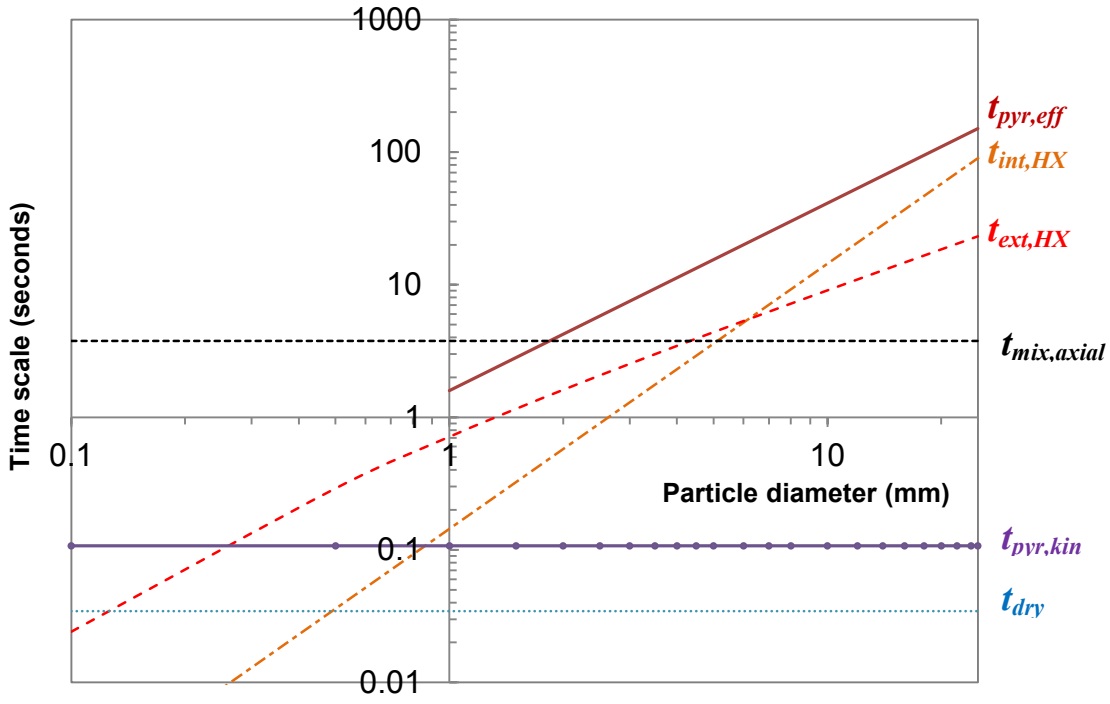

Figure 2 Time scales for particle devolatilization and mixing versus biomass particle diameter (in mm)

For particles larger than 6mm, time-scale of axial solids mixing t_{mix} is much faster than the overall pyrolysis time $t_{pyr,eff}$ meaning that the solids can safely be assumed as axially well-mixed before pyrolysis occurs. On the other hand, for particles smaller than 0.5mm, it can be assumed that the devolatilization occurs instantaneously at the feeding port, before they've had a chance to be fully mixed into the fluidized bed- a phenomena which has been observed experimentally and is considered by some models [84,85]. Intermediate sized biomass particles ($0.5mm<d_{bio}<6mm$) can be expected to undergo mixing and heat transfer processes simultaneously [86]. For this system, the computed lateral dispersion coefficient, D_L is $3.6*10^{-4}$ m^2/sec, is similar to that measured experimentally in Olsson et al. [87], and corresponds to a lateral mixing time-scale, $t_{mix,lateral}$ of ~15 seconds. The Damköhler mixing criterion as proposed by Leckner and Werther [80] is defined in equation (1),

$$Da_L = \frac{t_{mix,lateral}}{t_{pyr,eff}} \leq 1 \quad (1)$$

The criterion requires that biomass particles larger than 5mm be used to ensure adequate lateral mixing for this reactor geometry see Table 1. As the size of the fluidized beds are increased to industrial scales (d_{bed}~3meters) the importance of lateral/axial fuel mixing becomes more important [80]. For example, the axial mixing time-scale increases linearly with bed height, while the lateral mixing time-scale in the Borodulya correlation scales according to $t_{mix,lateral} \propto \left(u_0 - u_{mf}\right)^{-0.7} H_{mf}^{-0.65} d_{bed}^{1.5} g^{-0.15}$. Thus, in order to preserve this scaling criterion, larger particles must be utilized in larger diameter reactors.

The physical and chemical time-scales for the conversion of resulting char particles [14] occurs over a much longer time (100's-1000's of seconds) compared to the devolatilization processes and therefore can be modeled as two sequential events[45]. It has been previously shown

that steam gasification is limited by the gasification kinetics [14,71,88] while the combustion of particles is limited by a mixture of internal/external diffusion and kinetic resistances[14].

2.3.2. Gas phase chemical reactions

A large number of chemical reactions occur during fluidized bed gasification. Before undertaking model development, it is useful identify the potential rate-limiting processes, as well as those which contribute strongly to the energy balance. A global reaction offers an approximation of the effects of the many elementary reactions which actually occur [89] and is useful for estimating the time-scales of chemical reactions [90]. The assumptions and rate parameters used are summarized in Table 2. The rates and time-scales will depend strongly on the operating pressure, temperature and gas phase composition so for this analysis the outlet concentrations from a pilot scale steam blown fluidized bed gasifier were adopted [18,91]. The measured outlet concentration of oxygen was 0%, so for the purposes of the time-scale analysis a bed oxygen fraction of 5%vol was assumed as done by Leckner and Werther [80] in their scaling study.

Table 2 Summary of kinetic rates and assumptions for time scale analysis of chemical reactions during FBBG

Transport process or reaction	Characteristic time scale (sec) $t_j = C_j/R_j$ Reaction rates, R_j in $kmol_j/m^3/s$, concentrations, C_j in $kmol_j/m^3$ T in Kelvin, R_g, in J/mol/K	Heat of reaction	Source
Gas-phase global reaction		ΔH^0_{298} [kJ/mol]	
H_2 Oxidation $H_2+1/2O_2 \rightarrow H_2O$	$R_{H_2} = k_{H_2} C_{H_2} C_{O_2}^{0.5}$ $k_{H_2} = 5.69 * 10^{11} \exp(-146{,}408/R_g T)$	-241.9	Marinov et al. [92]
CO Oxidation $CO+1/2O_2 \rightarrow CO_2$	$R_{CO} = k_{CO} C_{CO} C_{O_2}^{0.25} C_{H_2O}^{0.5}$ $k_{CO} = 2.238 * 10^{12} \exp(-167{,}360/R_g T)$	-283	Dryer and Glassman [93]
CH_4 oxidation $CH_4+3/2O_2 \rightarrow CO+2H_2O$	$R_{CH_4} = k_{CH_4} C_{CH_4}^{0.7} C_{O_2}^{0.8}$ $k_{CH_4} = 5.0118 * 10^{11} \exp(-202{,}505/R_g T)$	-519.4	Dryer and Glassman [93]
CH_4 reforming $CH_4 + H_2O \leftrightarrow 3H_2 + CO$	$R_{CH_4-H_2O} = k_{CH_4} C_{CH_4}^{1.48} C_{H_2}^{-0.91} C_{H_2O}^{-0.11}$ $k_{CH_4-H_2O} = 1.488 * 10^4 \exp(-211{,}000/R_g T)$	201.9	Dufour et al. [94]
Primary tar cracking *Tars* $\rightarrow$ Light gases	$R_{tar} = k_{tar} C_{tar}$ $k_{tar} = 9.55 * 10^4 \exp(-93{,}288/R_g T)$	<0	Boroson et al. [95]
Secondary tar cracking $C_{10}H_8 \rightarrow 0.625C_{16}H_{10} + 0.785H_2$	$R_{tar} = k_{tar,2} C_{tar,2}$ $k_{tar,2} = 1.94 * 10^{13} \exp(-326{,}000/R_g T)$	N/S	Fuentes-Cano et al. [57]
Water gas shift $CO + H_2O \leftrightarrow H_2 + CO_2$	$R_{wgs} = k_{wgs}(C_{CO} C_{H_2O} - C_{CO_2} C_{H_2}/K_{WGSR})$ $k_{wgs} = 2.78 * 10^3 \exp(-12{,}560/R_g T)$ $K_{WGSR} = 0.0265 \exp(-3958/T)$	-41.2	Biba et al., [96] Souza-Santos [97]
Heterogeneous reactions			
Char combustion $C+1/2O_2 \rightarrow CO$	$R_{ch-O_2} = k_{ch-O_2} C_{O_2} C_c$ $k_{ch-O_2} = 1.5 * 10^9 \exp(-108{,}730/R_g T) \frac{R_g T}{101325}$	-110.6	[14,98]
Reactor properties			
Gas phase residence time	t_{bed} =*~0.5-0.7* sec $t_{freeboard}$ =*4-30 sec*		[99] [69,99]
Total concentration Concentration Assumed mole fractions	$C_{tot} = P/R_g T \frac{1}{1000} kmol/m^3/s$ $C_j = X_j C_{tot}\ P = 101325\ Pa$ $X_{CO} = 0.0737,\ X_{H_2} = 0.1205\ X_{H_2O} = 0.3585$ $X_{CO_2} = 0.1706\ X_{N_2} = 0.1918\ X_{O_2} = 0.05^*$		[18,91] [80]*

Care was taken to utilize a consistent and independently validated [100] system of hydrocarbon oxidation kinetics (i.e $R_{H_2}, R_{CO_2}, R_{CH_4}$). This is particularly important because the kinetics for even the simplest global reaction (hydrogen oxidation) display a wide scatter[45] depending on the source. For example some gasification models have applied global rate parameters which result in instantaneous hydrogen oxidation [26,101,102]. In other cases, the carbon monoxide oxidation kinetics have been modified by tuning factors [103] to produce agreement with data. The quantitative validity of single or two-step oxidation kinetics under such fuel-rich conditions is uncertain given that they are fitted under stoichiometric or lean conditions[92]; nevertheless, they can provide useful insight into the relative chemical stability of these hydrocarbons. The water gas shift kinetics refer to the commonly used expression from Biba et al. [50,96,97] which accounts for the catalytic effect of the bed material.

Figure 3 shows that the chemical reactions occur over a wide range of time scales. Methane steam reforming is shown to be the slowest and certainly negligible [26] under the expected total gas-phase residence times of 4-30 seconds [91,99]. The global conversion and dehydrogenation of naphthalene ($C_{10}H_8$) to produce larger polycyclic aromatic hydrocarbons (PAH's) (i.e. pyrene, $C_{16}H_{10}$) is also slow but significant at operating temperatures greater than 880°C. Primary tar cracking, water gas-shift, and methane oxidation all occur within typical residence times and would therefore demonstrate kinetic limitations. The oxidation reactions can be sorted from highest to lowest reactivity in the following way, $R_{H2} \geq R_{CO} \geq R_{CH4} \geq R_{ch\text{-}O2}$. Because of the high rates of these oxidation reactions, it is expected that the local concentration of oxygen will be small in the bed region- creating extremely fuel-rich conditions. Therefore, the actual oxidation rates need to be computed using comprehensive gas phase mechanisms which are valid across a range of equivalence ratios. Moreover, the relatively slow conversion of char by

oxidation and gasification reactions confirm their rate-limiting importance: these reactions result in a significant steady state char inventory and ultimately govern the size and/or maximum solids feeding rate for a gasifier [14].

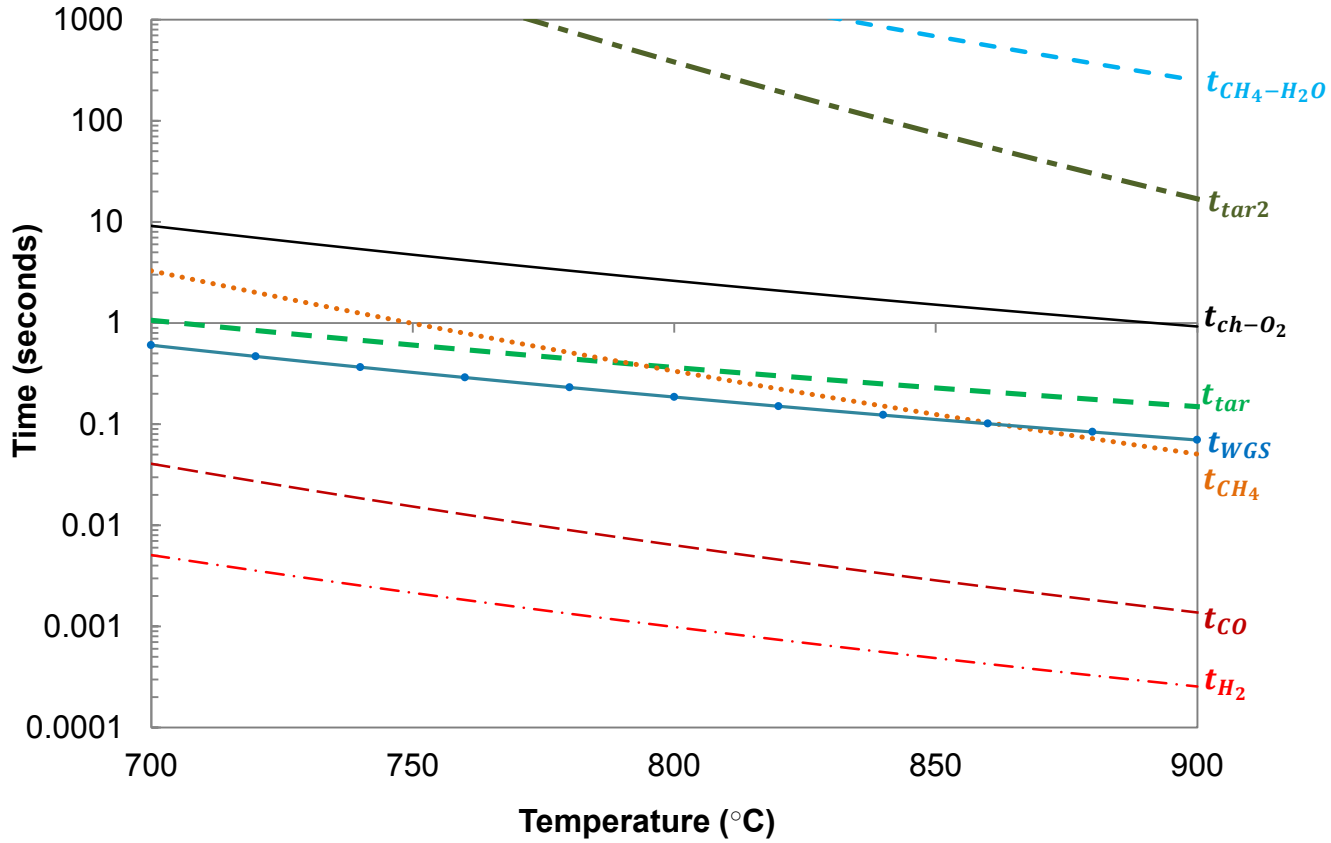

Figure 3 Time scale (seconds) of homogeneous and heterogeneous reactions during fluidized bed gasification versus temperature (°C)

To summarize, the results of the time-scale analysis, intermediate sized biomass particles between 0.5mm and 6mm are dominated by an external heat transfer resistance and expected to undergo axial mixing simultaneously. However, lateral segregation of volatiles may occur unless adequately sized particles are utilized: larger particles are required in larger diameter beds. The gas phase reactions occur over a range of time scales with methane appearing relatively resilient to conversion by steam under fluidized bed gasification conditions. Heterogeneous reactions (gasification/combustion) can be considered feed rate-limiting due to their relatively slow rates.

3. **Mathematical model**

In order to improve on the previous models in the literature, and based on the time scale analysis, a multi-scale, coupled reactor model (CRNM) is proposed which incorporates sub-models for i) particle-devolatilization ii) gas phase hydrodynamics and conversion, and iii) char conversion. These sub-models are discussed separately followed by a discussion of the coupling of all three sub-models.

3.1.Drying and devolatilization sub-model

Owing to the large fraction of volatiles released during biomass devolatilization (70-90% initial wt dry), model predictions for outlet gasifer concentrations are highly sensitive to the applied kinetic sub-model [50,58,63]. As such, the present particle devolatilization sub-model utilizes the most up to date primary pyrolysis mechanism proposed by the CRECK modeling group (Debiagi et al., 2015) [104] which describes biomass degradation as a linear superposition of its macromolecular components including hemicellulose ($C_5H_8O_4$), cellulose ($C_6H_{10}O_5$), LIGC

($C_{15}H_{14}O_4$), LIGH ($C_{20}H_{22}O_{10}$) and LIGO ($C_{22}H_{28}O_9$). In this study, the extractive species are neglected. Given the feedstock's ultimate analysis, hemicellulose and cellulose content, the initial fractions of LIGC, LIGH, and LIGO are computed by solving a system of equations. The 26 reaction mechanism is comprised of 43 species including 19 solid, 23 gas, and one liquid (moisture). Because of the fast rate of devolatilization, the steady state inventory of biomass particles is negligible compared to the char and inert bed material inventories.

The residual char is described by eight species: pure carbon and seven metaplast species (CO,H_2, CO-H_2,CO_2, CH_4,CH_3OH, and C_2H_4). The release of these trapped components into the gas-phase occurs slowly compared to the other devolatilization reactions necessitating their inclusion in the char phase.

As identified in the time-scale analysis, the dominant heat transfer resistance for millimeter-scale particles is external. For actively pyrolyzing particles, mass transfer occurs rapidly outward and is driven by the increased internal gas pressure from freshly formed volatile products [105]. As a result, intraparticle reactions are neglected and the particles can be assumed to be internally uniform- heating up according to the following time varying temperature profile,

$$T_{bio}(t) = T_r - \left(T_r - T_{bio,0}\right)\exp\left(-t/t_{ext,HX}\right) \quad (2)$$

where T_r is the reactor temperature in K, $T_{bio,0}$ is the initial temperature of the biomass entering the reactor, and characteristic time-scale for heat transfer $t_{ext,HX}$ is identical to that shown in Table 1.

$$t_{ext,HX} = \rho_{bio} c_{p,bio} d_{bio}/(6h_{avg}) \quad (3)$$

As shown in Gomez-Barea et al. [72], the effective external heat transfer coefficient experienced by an actively devolatilizing particle in a fluidized bed can be estimated by averaging gas-solid and solid-solid heat transfer coefficients,

$$h_{avg} = (h_s + h_f)/2 \quad (4)$$

Where, the solid-solid Nusselt number Nu_s is computed based on the inert particle properties [45,73]

$$Nu_s = h_s d_p / k_f = 0.85 Ar^{0.19} + 0.006 Ar^{0.5} Pr^{1/3} \quad (5)$$

And the gas-solid heat transfer coefficient is,

$$Nu_f = h_f d_{bio} / k_f = 2 + 0.6\left(Re_{mf,bio}/\varepsilon_{mf}\right)^{0.5} Pr^{1/3} \quad (6)$$

where the Reynolds number Re_{mf} depends on minimum fluidizing velocity of the bed material u_{mf} and the biomass particle diameter,

$$Re_{mf,bio} = \rho_f u_{mf} d_{bio} / \mu_f \quad (7)$$

3.2.Gas phase hydrodynamics and conversion

A complete description of the hydrodynamics in a reacting fluidized bed must consider both the i) gas-phase mixing patterns and ii) distribution of volatiles released by the active solid phases. These quantities are difficult to predict because of the large number of interparticle collisions, gas-solid drag forces, and potential spatial segregation of the multiple solid phases including biomass, ash, and char particles [45,106]. Many fluidization models (FM) have adopted the two-phase theory of fluidization in which the bed is dichotomized into i) a dense phase, also known as emulsion, ii) a bubble phase of low solids concentration iii) and a throughflow phase. This approach requires empirical correlations to describe the transfer of gases between the phases. However, as noted by Gomez-Barea and Leckner [25], aside from sharp gradients at the distributor, most of the bed exists with spatially uniform gas concentrations and temperature, consistent with a well-stirred assumption. Sridhar [107] compared RNM predictions using the two-phase theory and WSR emulsion phase, showed that well-mixed assumption was valid under bubbling bed, steam-blown conditions. Under air-blown conditions however, RNM predictions were sensitive

to the assumed volatile release patterns. In this study we adopt the same reactor network model (RNM) utilized by Stark et al. [58] shown in Figure 4.

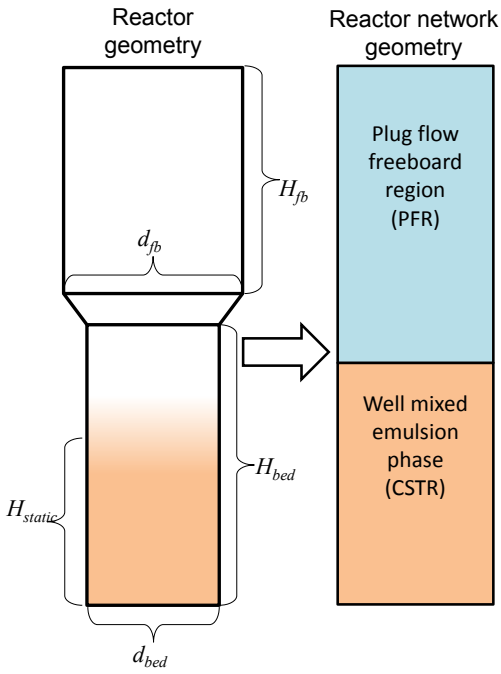

Figure 4 Reactor network geometry derived from actual geometry

Biomass and char phases are assumed to be well-mixed in the emulsion phase. The reactor is divided into two reactors in-series, whose volumes are computed from the known geometric and operational inputs combined with assumptions derived from the two-phase theory of fluidization (for details see Appendix 1). We adopt the same secondary gas phase conversion mechanism used in our previous study [58] developed by the CRECK group which consists of 327 species and 10933 reactions. As identified in the literature [58,108], the water gas-shift reaction kinetics are modified in the bed region to account for the catalytic impacts of minerals with the expression from Gomez-Barea & Leckner [26].

In this study, a custom solver for the reactor network has been written in MATLAB. Cantera [109], an open-source software package, is used to interpret the input chemical kinetic mechanism and thermodynamics data.

3.2.1. Continuously stirred tank reactor (CSTR)

The unsteady conservation of species equations for an isothermal, isobaric continuously stirred tank reactor (CSTR) are given by,

$$V\frac{dC_j}{dt} + \dot{V}_{out}C_j - \dot{V}_{in}C_{j,in} = \dot{\omega}_j V + F_{j,ch}\ (j = 1,2..N_s) \tag{8}$$

where N_s is the total number of species, V is the gas phase volume of the reactor in (m_{gas}^3), $\dot{V}$ refers to the volumetric flow rate (m^3/sec), and $\dot{\omega}_j$ is the net production rate (mol/m^3/sec) of the j^{th} species due to homogeneous reactions computed from the gas phase mechanism stoichiometric coefficients and rate of progress variable for each reaction[110]. $F_{j,ch}$ is the net production rate due to heterogeneous reactions in mol/sec, and is computed by the char conversion submodel. The equation of state for an ideal gas gives the total concentration (C_{tot}) in mol/m^3,

$$C_{tot} = \frac{P}{R_g T} = \sum_{j=1}^{N_s} C_j \tag{9}$$

where P is the pressure in Pa, T is the temperature in K, and R_g is the ideal gas constant in J/mol/K. Combining this with the unsteady conservation of mass (continuity) provides a closure equation for the outlet volumetric flow rate of the CSTR.

$$V\frac{dC_{tot}}{dt} + \dot{V}_{out}C_{tot} - \dot{V}_{in}C_{tot} = \sum_{j=1}^{N_s}(\dot{\omega}_j V + F_{j,ch}) \tag{10}$$

In this study, the bed region is assumed to be isothermal at the experimentally measured/specified temperature. In general however, the conservation of energy for a constant volume well stirred reactor can be written,

$$\frac{dT}{dt} = \frac{\dot{Q}_{in} + \sum_{j=1}^{N_{in}} \dot{m}_{j,in}(h_j) - \sum_{j=1}^{N_{out}} \dot{m}_{j,out}(h_j)}{m\bar{c}_v} \tag{11}$$

where, N_{in} represents the number of input streams which may include raw biomass and fluidizing agent (steam and or air), N_{out} represents the number of outlet streams which include attrited/elutriated carbon/ash computed by the char submodel, as well as N_s gas phase species. The total specific enthalpy is given by the summation of the formation enthalpy and sensible enthalpy,

$$h_i(T) = \overset{\circ}{h}_{f,i} + \int_{T_0}^{T} c_{p,i}\,(T)dT \tag{12}$$

where $\overset{\circ}{h}_{f,i}$ is the standard heat of formation of species *i* in J/kg and $c_{p,i}$ is the specific heat capacity of component *i* in J kg^{-1} K^{-1}, and T_0 is the standard temperature (298.15K).

Combining the steady form of the species conservation and energy equations results in a non-linear algebraic system of N_s+1 equations which are solved by the `optimset` MATLAB function using the Levenberg-Marquardt algorithm. However, in order to robustly achieve convergence, the non-linear solver requires an appropriate initial guess for the vector of concentrations and temperature. The initial guess is produced by solving the transient system of

non-linear ordinary differential equations (ODE's) for a sufficiently large multiple of gas residence times.

3.2.1. Plug flow reactor

For an isobaric, one dimensional (1D) plug flow reactor with variable gas density the unsteady conservation of species equations are,

$$\frac{dC_j}{dt} + \nabla \cdot \left(C_j u\right) = \dot{\omega}_j \; (j = 1,2..N_s) \tag{13}$$

Assuming negligible pressure drop across the reactor, the continuity equation provides closure on the flow velocity,

$$\frac{dC_{tot}}{dt} + \frac{d}{dz}(C_{tot}u) = \sum_{j=1}^{N_s} \dot{\omega}_j \tag{14}$$

Where *u* refers to the superficial flow velocity in m/s. Applying the steady-state assumption, and writing the spatial coordinate (z) in terms of the flow packet residence time τ and velocity,

$$\frac{dz}{d\tau} = u \tag{15}$$

In this study, the system/freeboard is assumed to be isothermal at the experimentally measured temperature. In general however, the conservation of energy for a constant pressure plug flow reactor can be written,

$$\frac{dT}{d\tau} = \frac{1}{\rho \bar{c}_p}\left(\frac{1}{A_c}\frac{d\dot{Q}_{in}}{dz} - \sum_{j=1}^{N_s} \dot{\omega}_j MW_j h_j\right) \tag{16}$$

Where $\dot{Q}_{in}$ is the net external heat input per unit length in W/m and $\bar{c}_p$ is the mixture-averaged constant pressure specific heat capacity in J/kg/K. In the non-isothermal case, the equation of state for an ideal gas is required for closure of the continuity equation.

$$\frac{dC_{tot}}{d\tau} = -\frac{P}{R_g}T^{-2}\frac{dT}{d\tau} \tag{17}$$

3.2.2. Gasifier energy balance, efficiency

The steady-state conservation of energy equation (see equation (11) across the entire gasifier control volume is used to compute a net heat demand in Watts,

$$-\dot{Q}_{in} = \sum_{j=1}^{N_{in}} \dot{m}_{j,in} h_j - \sum_{j=1}^{N_{out}} \dot{m}_{j,out} h_j \tag{18}$$

The cold gas efficiency based on the higher heating value (HHV) of all gas phase components divided by the heating value of the fed biomass,

$$\eta_{HHV} = \frac{\sum_{j=1}^{N_s} HHV_j \dot{m}_{j,out}}{HHV_{bio} \dot{m}_{bio}} \tag{19}$$

where the (HHV) of the biomass is computed from its ultimate analysis [105] while the gas phase component HHV's are computed from their standard enthalpies of formation using a separate routine.

3.3.Char conversion

The char conversion model augments the one recently developed by Bates et al. in ref. [14]. For brevity, not all the equations are reproduced here and readers are encouraged to see the original paper for more details. Briefly summarized, the model considers two classes of particles: i) the mother char particles are formed by the primary fragmentation of raw biomass ii) and the attrited fines are assumed to be elutriated as soon as they are produced. The transient conversion sub-model solves conservation equations (ODE's) for the mother char particles' average properties (size, density, mass), accounting for the competing consumption pathways including gasification, combustion, and attrition. The sub-model takes the gas-phase environment, temperature and pressure as inputs. Then, the residence time distribution for char particles is solved for iteratively, and used to output the steady-state char statistics (see Figure 5).

Notably, the previous model described char as a mixture of carbon, ash, and void, whereas in this study the carbonaceous fraction of the char also consists of the residual metaplast species from the primary pyrolysis mechanism employed [104],

$$\rho_{ch} = \rho_c + \sum_{k=1}^{N_t} \rho_k \tag{20}$$

Where k refers to the trapped gas species, (k=CO,H_2, CO-H_2,CO_2, CH_4,CH_3OH, and C_2H_4) and and N_T is the number of metaplast species (in this case, seven). The density of the individual trapped gases depends solely on their respective release kinetics,

$$\frac{d\rho_k}{dt} = -R_{release,k}\rho_k \ (k = 1,2..N_T) \tag{21}$$

It has been assumed that attrition and combustion reaction on the surface of the particle also contribute to the release of metaplast species into the gas phase,

$$\frac{dm_k}{dt} = -\left(R_{att} + R_{comb} + R_{release,k}\right)m_k \ \ (k = 1,2..N_T) \tag{22}$$

These add to the equations (6,7,8) in ref. [14]).

3.4.Solution procedure

The coupled reactor network model (CRNM) predicts the steady-state gasifier outputs including gas phase concentrations, and solids statistics (conversion, inventory) by incorporating the simultaneous solution of three sub-models. This sequential modular approach enables the individual sub-models to undergo tuning, validation, and sensitivity analysis separately from the reactor model. The overall solution algorithm is shown in Figure 5.

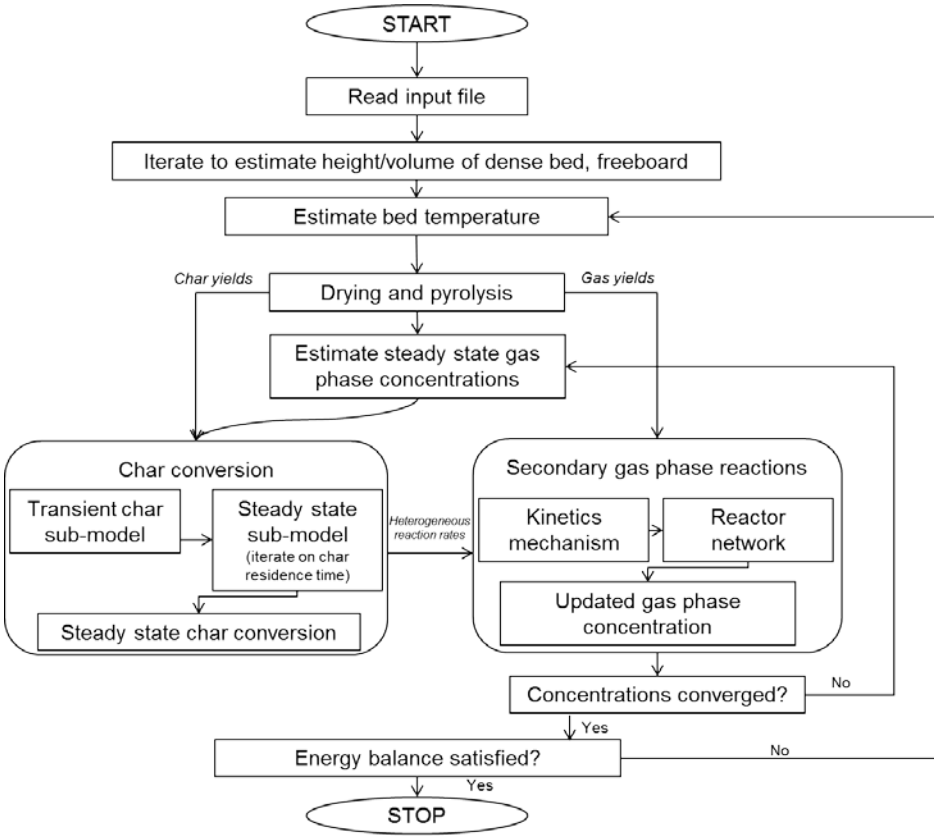

Figure 5 Couple reactor network model (CRNM) solution algorithm

Hydrodynamic calculations compute the initial reactor volumes for the gas phase conversion model. If the reactor temperature is known, it is used as an input to the particle devolatilization model, otherwise the net heat input must be specified and an outer energy balance convergence loop must iterate on the temperature variable until equation (18) is solved. The particle devolatilization model outputs i) a vector of species mass flow rates to the gas-phase conversion model ii) the production rate and solids composition to the char conversion model. The inner convergence loop generates an initial estimate for the bed concentrations by solving the secondary gas phase reactions without char reactions. This estimate is an input to the char submodel which outputs a steady-state net production rate vector,$F_{j,ch}$, from heterogeneous reactions. The gas phase conversion model is solved again with the updated net production rate vector. These steps repeat until the gas phase concentrations in the bed converge using a damped iterative method.

4. **Experimental methods**

4.1.Materials

Gasification experiments were conducted using white oak (*quercus alba*) and New England hardwood (NEHW) in a pilot-scale facility shown schematically in Figure 6. The NEHW feedstock was prepared (ground) from wood pellets manufactured by New England Wood Pellet©. Both feedstocks were sieved to a +10/-25 mesh (725μm<d_{bio}< 2mm). The proximate and ultimate analyses of the oak and New England Hardwood (NEHW) feedstock are shown in Table 3. The carbon, hydrogen, and nitrogen mass fractions were determined using a LECO

TruSpec CHN module. Proximate analysis values (moisture, volatiles, fixed carbon, and ash) were determined using a LECO TGA701 Thermogravimetric Analyzer.

Table 3 Proximate, ultimate analysis, and model parameters for feedstocks employed

Feedstock	Oak	New England Hardwood	Source
Proximate analysis(%weight as received)			
Loss on drying	3.95	4.3	
Voltatile matter	84.79	78.84	
Fixed carbon	10.9	16.26	
Ultimate analysis (%weight dry basis)			
Carbon	48.1	47.73	
Hydrogen	6.25	6.49	
Oxygen	45.17	45.01	
Nitrogen	0.06	0.1	
Sulfur	0.052	0.07	
Ash	0.37	0.6	
Higher Heating value (MJ/kg dry)	19.14	19.35	
Fiber analysis (%wt dry)			
Cellulose	35 ref. [111]	36 (Measured)	
Hemicellulose	40 ref. [111]	41.75 (Measured)	
LIG (by difference)	25	22.2	
LIGC (computed)	0.99	3.07	
LIGH (computed)	9.85	8.47	
LIGO (computed)	14.17	10.67	
Assumed feedstock model parameters			
$d_{bio,0,}$ mean particle diameter (m)	$1.375*10^{-3}$	$1.375*10^{-3}$	Measured
$\rho_{bio,}$ apparent biomass particle density (kg/m^3)	820	820	[81]
$cp_{bio,}$ specific heat capacity (J/kg/K)	1112+4.85T	1112+4.85T	[112]
Shape (cylinder, slab, sphere)	Slab	Slab	
φ, shrinkage factor (m^3/m^3)	1.68	1.68	[49]
n_1 primary fragmentation factor (-)	3	3	[14]
q, structural attrition constant (-)	2	2	[14]
$K_{att,0}$ initial attrition constant (-)	$0.8*10^{-7}$	$0.8*10^{-7}$	Measured
ψ Reactivity factor (-)	0.24	0.24	[14]

Table 3 also summarizes the parameters required for the particle scale devolatilization and char conversion models. Where possible, the feedstocks parameters were measured directly, but, if this was not possible, values were taken from similar feedstocks in the literature.

4.2.Facility

Gasification experiments were carried out in an integrated gasification system, with coupled solids feeding, gasification reactor, solids disengaging, liquid scrubber, condensate removal, and non-condensable gas filtration and analysis (see Figure 6). The heart of the gasification system is a four inch (10.2 cm) inner diameter Incoloy 800 reactor with a 6 inch (15.4 cm) freeboard disengaging section directly above the reactor. Biomass is fed to the reactor through a feed arm at a 45° angle to the reactor approximately 20.3cm above the gas distributor plate. Biomass is metered using a loss-in-weight feed hopper (K-tron) that delivers biomass at rates between 0.5 to 1.5 kg hr^{-1}. Metered biomass is then pneumatically transported using humidified nitrogen and an eductor pump to the top of a lock hopper. The lock hopper consists of two ball valves that rotate on a pre-set schedule to charge biomass onto a continuously rotating auger (Baldor, 360 rpm). The auger transports the biomass to the top of the bubbling fluidized bed.

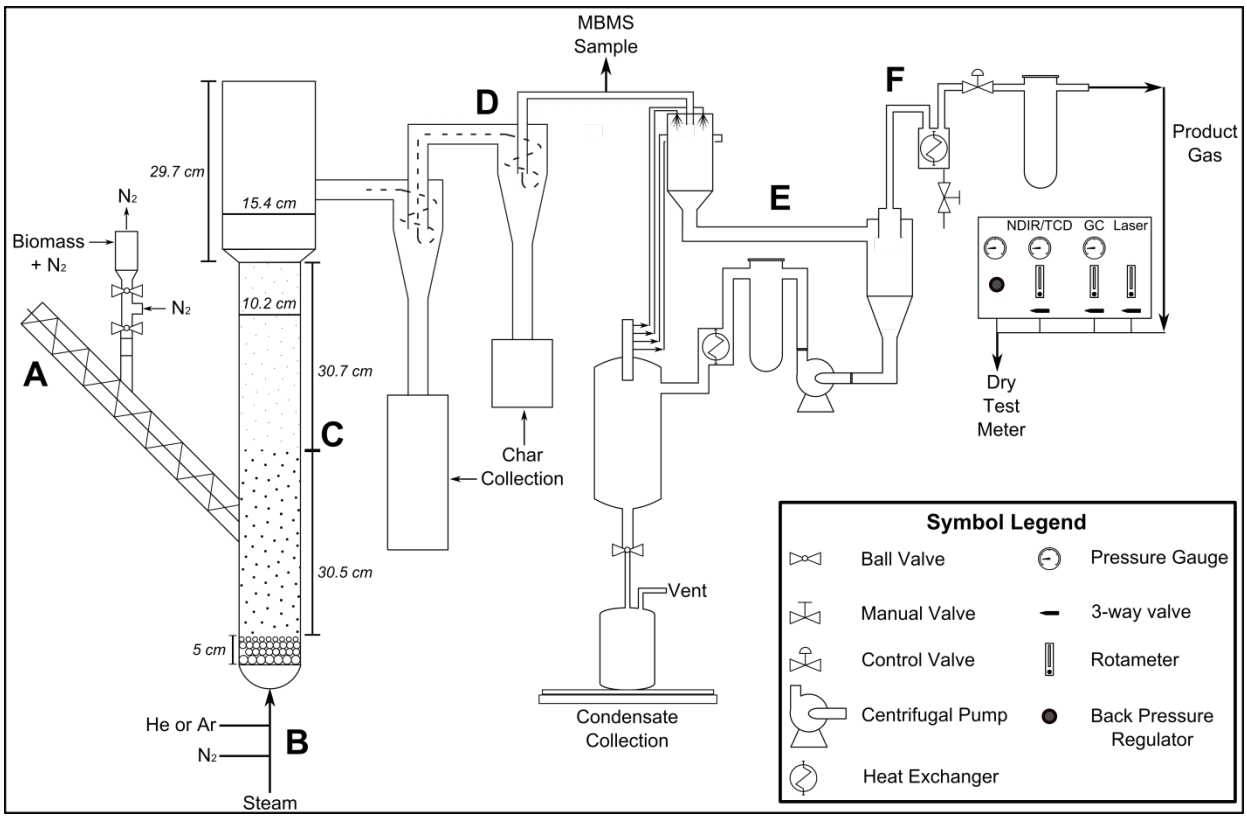

Figure 6 Schematic of 4inch bench scale steam/air blown gasification reactor, sampling, collection, and characterization equipment A, pneumatic screw feeding system, B- fluidization agent preheating system C- gasifier D solids capture system E- scrubber system, F- gas filtration and sampling system

Olivine sand (AGSCO Corp., 3 kg) with an average particle diameter of 270μm is fluidized with steam generated by a Sussman stainless steel electric boiler. For this study, steam flow rates varied between 0.8 – 1.2 kg/h. During air gasification tests the steam volume was supplemented with air and/or nitrogen flow metered by Teledyne-Hastings mass flow controllers. A superheater coil below the bubbling fluidized bed pre-heats incoming steam or air to the desired gasification temperature prior to entering the bed.

Argon and helium tracer gas flow was controlled using an MKS Instruments mass flow controller. Temperature in the bed was controlled using internal thermocouples and thermocouples close to the heating elements. Solids were removed with dual stage char cyclones, and char was cooled, collected, and weighed. Solid-free hot vapors (> 400°C) were analyzed using the molecular beam mass spectrometer (MBMS) [113], and then cooled to room temperature in a recirculating wet scrubber system. Condensate was collected into a drum continuously and monitored using a level-sensor, while non-condensable gases were filtered to 2 μm and then analyzed.

Analysis of H_2, CO, CO_2, CH_4, and O_2 gases was accomplished using non-dispersive infrared detectors (NDIR, CAI) and a hydrogen thermal conductivity detector (H_2-TCD, Nova). An Opto 22 control system was used to read in process data including NDIR and TCD measurements, and was used to control all aspects of the experiment. Quantitative gas analysis was carried out using an Agilent 7890A gas chromatograph (GC) paired with a Wasson ECE heated valve box. The GC is equipped with dual TCD and dual FID detectors and is capable of measuring all non-condensable gas species (e.g. He, Ar, N_2, H_2, CO, CO_2, CH_4) and trace amounts of benzene. Quantitative tar analysis from data collected using the MBMS was achieved

by adding a pre-mixed tar standard to the stream at a known flow rate and measuring the response factors for benzene, toluene, phenol, naphthalene, phenanthrene, and pyrene.

Particle size distribution analysis on the collected solids was performed by laser diffraction using a Malvern Mastersizer 2000 with methods developed using char standards. Sample particles were admitted into a measured flow cell in front of a laser beam, and the intensity of light scattered by the particles was measured. The scattered light pattern was analyzed to calculate the particle size distribution, and results are given in terms of volume fraction across a particle size range (0.2 μm – 2000 μm).

4.3.Operating conditions

Table 4 summarizes the operating parameters varied during this study.

Table 4 Summary of experimentally defined or measured operating conditions

Fluidizing agent	Feedstock	T_{bed}	T_{FB}	Pressure	Feed rate (FR)	Steam/biomass ratio (SBR)	Air/fuel equivalence ratio (ER)	Superficial gas velocity (u_0)
		°C	°C	Pa (abs)	kg/hr	kg_{H2O}/kg_{Bio}	$mol_{O2}/mol_{O2stoich}$	m/s
Steam	Oak	750	750	117000	0.8	1	0	0.11
Steam	Oak	800	820	117000	0.8	1	0	0.115
Steam	Oak	850	850	117000	0.8	1	0	0.12
Steam	NEHW	750	765	117000	0.8	1	0	0.11
Steam	NEHW	800	815	117000	0.8	1	0	0.115
Steam	NEHW	850	865	117000	0.8	1	0	0.12
Air/Steam	Oak	850	850	117000	1.1	1.091	0	0.18
Air/Steam	Oak	850	850	117000	1.1	0.909	0.052	0.18
Air/Steam	Oak	850	850	132000	1.1	0.727	0.104	0.16
Air/Steam	Oak	850	850	117000	1.1	0.545	0.157	0.18

T_{bed} refers to the average temperature of the three thermocouples inserted to the center of the bed at heights of 7,12, and 17cm above the gas distribution plate. T_{FB} refers to the temperature of the freeboard measured at the wall, 70.2cm above the distributor. These are used as inputs for the gas phase conversion model and correspond to the CSTR and PFR temperatures, respectively.

The experimental conditions were carefully chosen so that the effects of several operating variables (temperature, feedstock, and air/fuel equivalence ratio) could be understood and disaggregated. This was done through a set of parametric experiments where only a single variable was modified at a time. The first six experiments examined the impact of temperature between 750-850°C for the two different feedstocks at a fixed steam to biomass ratio (SBR) of 1 and superficial gas velocity of approximately 0.115m/s. A separate set of four experiments examined the impact of air injection at a slightly higher biomass feed rate of 1.1kg/hr. In these experiments the superficial gas velocity in the bed was maintained between 0.16 and 0.18 m/s by reducing the steam to biomass ratio as the ER is increased.

5. **Results and discussion**

First, the impact of temperature on major gas species and tar composition is compared under steam blown conditions for the two different feedstocks. Then the influence of air injection on the major gas species and char elutriation is addressed in detail for the oak fed gasification conditions. Lastly, the impact of the operating conditions on important gasifier performance metrics is summarized.

5.1. Influence of temperature

5.1.1. Major gas species

In Figure 7a-f the influence of operating temperature on the outlet major gas species is compared for the oak and hardwood feedstocks. These eight components account for approximately >99%vol (on an inert free basis) of all measured species. The uncertainty for measurement of major gas species using gas-chromatography is +/-2% on the calibrated molar flow rates (mol/min) and are represented in the error bars found in the figures.

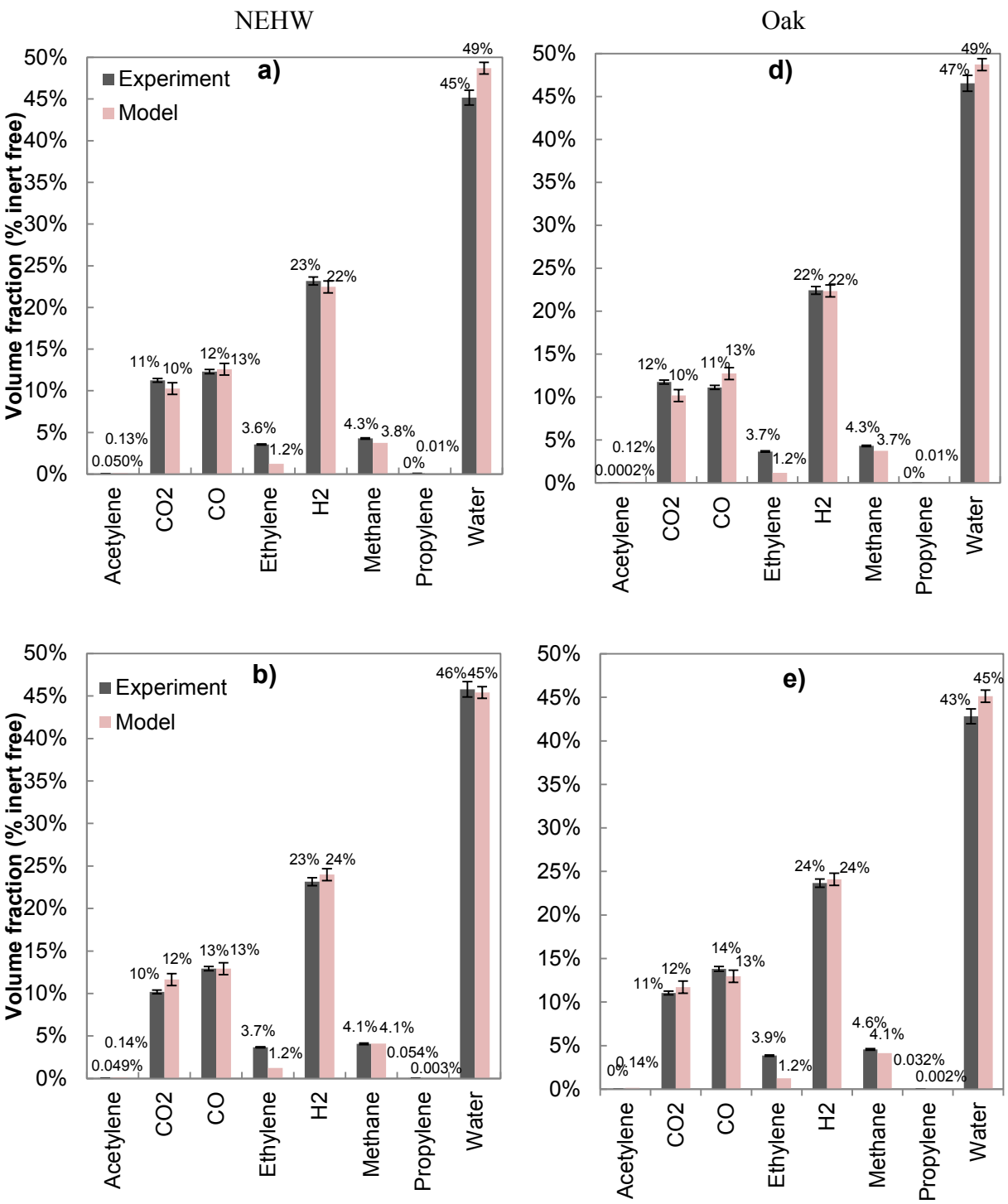

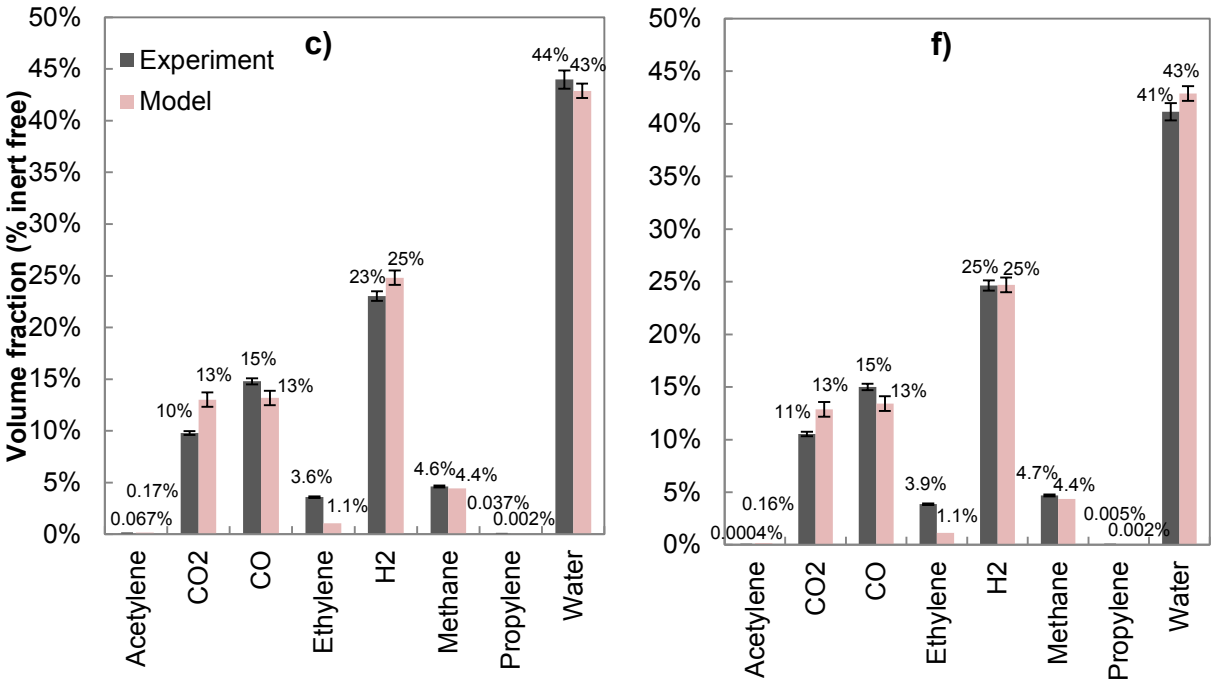

Figure 7 Concentration of major gas species (%vol. inert free) versus bed temperature during steam gasification. a-c) corresponds to NEWH, (d-f) corresponds to oak at bed temperatures of 750,800,850°C, respectively.

The differences in the major gas species produced by the two feedstocks appear to be minimal. Aside from the NEHW feedstock demonstrating a higher acetylene concentration (0.04-0.06 %vol inert free) compared to the oak feedstock (<0.0002 %vol inert free), the remaining species are not significantly different across the range of temperatures. The model predictions agree with the experimental data within the uncertainty ranges except for ethylene and propylene which are under-predicted.

One of the more significant trends among both feedstocks is the decrease in the steam concentration with increasing temperature. This can be explained by the promotion of the heterogeneous char-steam gasification reaction and water-gas shift. The model predictions show that the conversion of the carbon fraction of the char increases from 39% to 73% with increasing temperature. The overall conversion of the char (which includes the release of trapped gas components) is predicted to increase from 75% at 750C to 88% at 850C

The steam gasification reaction also explains the increase in H_2 and CO content which the model predicts rising from 22.5% to 24.5% and 12.5 to 13.5% respectively from 750 to 850 $^{\circ}$C. The experiments also demonstrate an increasing CO trend although they reach a higher volume fraction (~15%vol) than the model predictions (13.5%) at the highest temperature. Experimentally, the CO_2 fraction actually appears to remain constant or even decrease with temperature. Meanwhile, the model predicts that CO_2 increases with temperature. In order to explain the trends of CO_2 a discussion is necessary on the impact of the observed water gas shift reaction WGSR equilibrium coefficient defined as,

$$K_{WGSR,obs} = \frac{C_{CO_2} C_{H_2}}{C_{CO} C_{H_2O}} \tag{23}$$

The temperature dependence of this equilibrium constant is shown in Table 2, and is expected to decrease with increasing temperature. The WGSR equilibrium coefficient versus temperature for

the experimental data (points) and model predictions (dashed line) are shown in Figure 8. Neither the model nor the experiments show that the gas phase has reached equilibrium- confirming the strong kinetic limitations of this reaction raised in the previous time-scale analysis. The model shows that the approach to equilibrium is more likely at higher temperatures- consistent with increasingly faster reaction kinetics. Meanwhile the experimental WGSR data show a slightly decreasing water gas-shift with increasing temperature. The observed approach to equilibrium (defined by $K_{WGSR,obs}/K_{WGSR,}$) appears relatively constant versus temperature, ranging between 0.37-0.47 whereas the model predictions increase from 0.3-0.6.

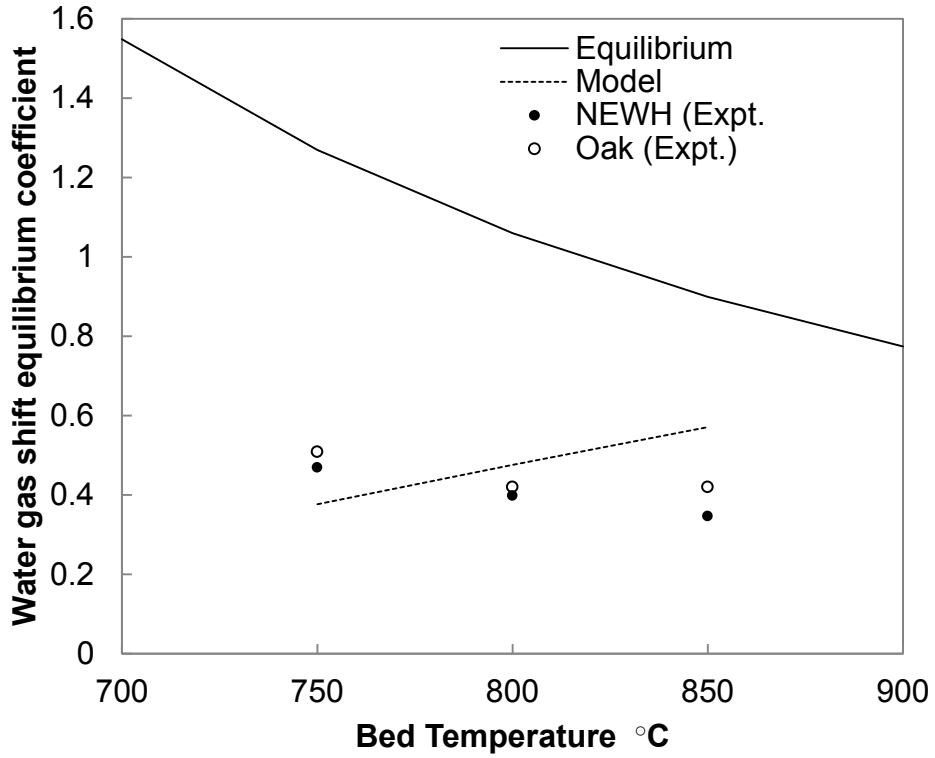

Figure 8 Water gas shift equilibrium coefficient K_{wgsr} [-] versus bed temperature in °C.

One possible explanation for this trend is that the WGSR is known to depend on the catalytic impact of the inorganics material contained in the char, which builds up to significant quantities once steady-state conditions have been reached [58,108]. The model accounts for this catalytic effect by using a faster rate in the bed region [25] and a non-catalytic rate in the freeboard region[58]. However, the model also predicts that the char inventory in the bed decreases by an order of magnitude from 243 grams of carbon to ~20 grams of carbon. Therefore, it should be expected that the magnitude of the catalytic acceleration should depend on the amount of catalytic material in the bed. Further experiments quantifying the dependence of WGSR as a function of amount and type of inorganics contained in the bed would be required to robustly describe this effect.

Additionally, there are several possible sources of error in experimentally measuring the major gas species components. Because liquid water is condensed before sampling in the GC/MS train, its production rate was estimated from periodically weighing the collected condensate. In some cases, inaccurate calibration for the level sensor as well resulted in erroneous condensate collection rates. Therefore, in these cases, the actual outlet steam flow rate was calculated to satisfy overall hydrogen and oxygen balances.

Another source of error that has been highlighted in previous studies [22] is that fluidized bed gasifiers demonstrate an initial transient behavior due to the build-up of char material which may take several hours depending on the conditions. Care was taken to run the experiments enough time to reach steady state where the major gas-species did not continue to change. Furthermore, during some runs, temporary feed interruptions were experienced which could have also impacted the steady-state assumption.

5.1.2. Tar species

Figure 9 shows the influence of temperature (750,800,850 °C) measured and predicted on the concentration of tar species during the oak steam gasification experiments (#1,#2,#3) See Table 6 in Appendix 2 for the definition of these tars. The experimental uncertainty was ±5% for the individually calibrated species and ±20% for the lumped mass calibrations ("other" and "heavy" tars). The "Total" tar concentration was computed by summing the mole fractions of the individually calibrated species (excluding benzene) and the lumped tar species [114].

Phenol and cresol are class 2, aromatic, water-soluble hydrocarbons and both demonstrate sensitivity to temperature with their concentrations decreasing rapidly from 700-850°C. Benzene appears relatively resilient to the increase in temperature. The model appears to consistently overpredict the benzene concentration by 0.2%vol, meanwhile, it under predicts cresol and pyrene.

Other temperature trends are well captured by the model although the quantitative agreement may be imperfect or within the uncertainty ranges. For example, the experiments demonstrate a gradual increase in naphthalene concentration from 108ppm to 122ppm whereas the model shows a more rapid increase from 27ppm to 126ppm at 750 and 850°C, respectively. The increase in phenanthrene is also well predicted by the model. The behavior of "other" tars is predicted relatively well, decreasing from 650ppm to 99ppm, agreeing with the experimentally observed reduction from 429 to 106ppm. Heavy tars are well predicted at 750°C but appear to be under predicted at higher temperatures. The model predictions agree well with the experimental trend showing "Total" tar concentrations (excluding benzene) decreasing monotonically with elevated temperatures.

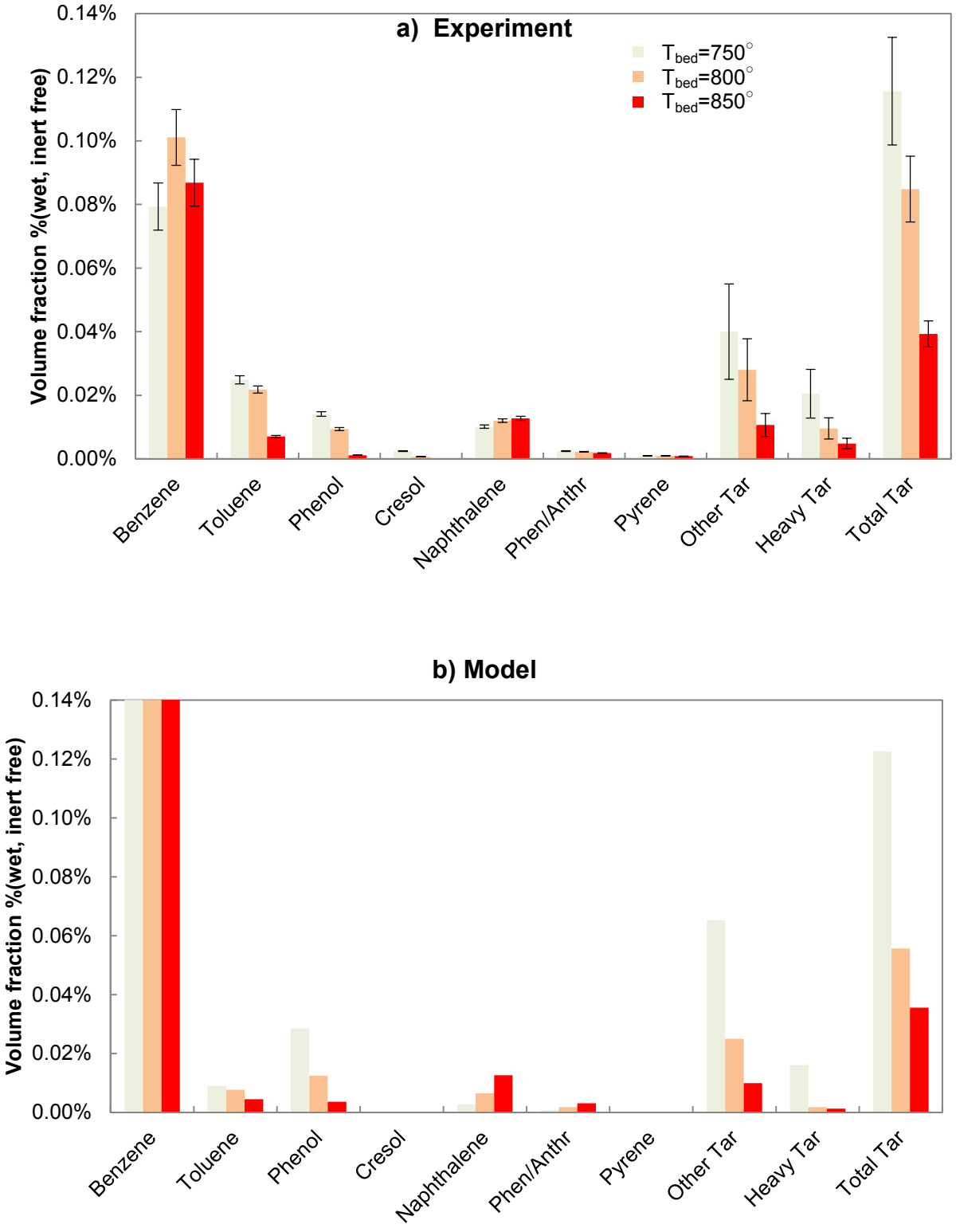

Figure 9 Concentration of tar species (%wet, inert free) versus temperature measured during experiments a) and predicted by model b) under steam-blown oak gasification conditions.

5.2.Influence of air fuel equivalence ratio

In the following section the feedstock (oak) and bed temperature (850°C) are held constant while the impact of the air/fuel equivalence ratio (ER) is assessed by varying it from 0 (steam only) to 0.157. In order to maintain a constant superficial gas velocity, the SBR was proportionally reduced (see Table 4).

5.2.1. Major gas species

Figure 10a-d show the impact of varying ER on the major gas species concentrations (%vol dry and nitrogen free basis) for the experiments #7-10. Note these are shown on a dry basis in order to highlight the trends with equivalence ratio.

Both the model and experiments show a drastic increase in the CO fraction as additional air is added to the system. This is explained by the additional char oxidation reaction (whose significance is proven in the next section). Beyond this ER=0.052, however, the CO concentration is relatively stable, suggesting that while the additional air may oxidize some additional char, this is offset by the oxidation of the CO itself. Interestingly, the experiments show that yield of ethylene increases drastically by 120% from 2.2% to 4.8% (vol dry) as ER increases from 0 to 0.052. Meanwhile, the model predicts that the ethylene concentration is actually reduced by the introduction of additional air.

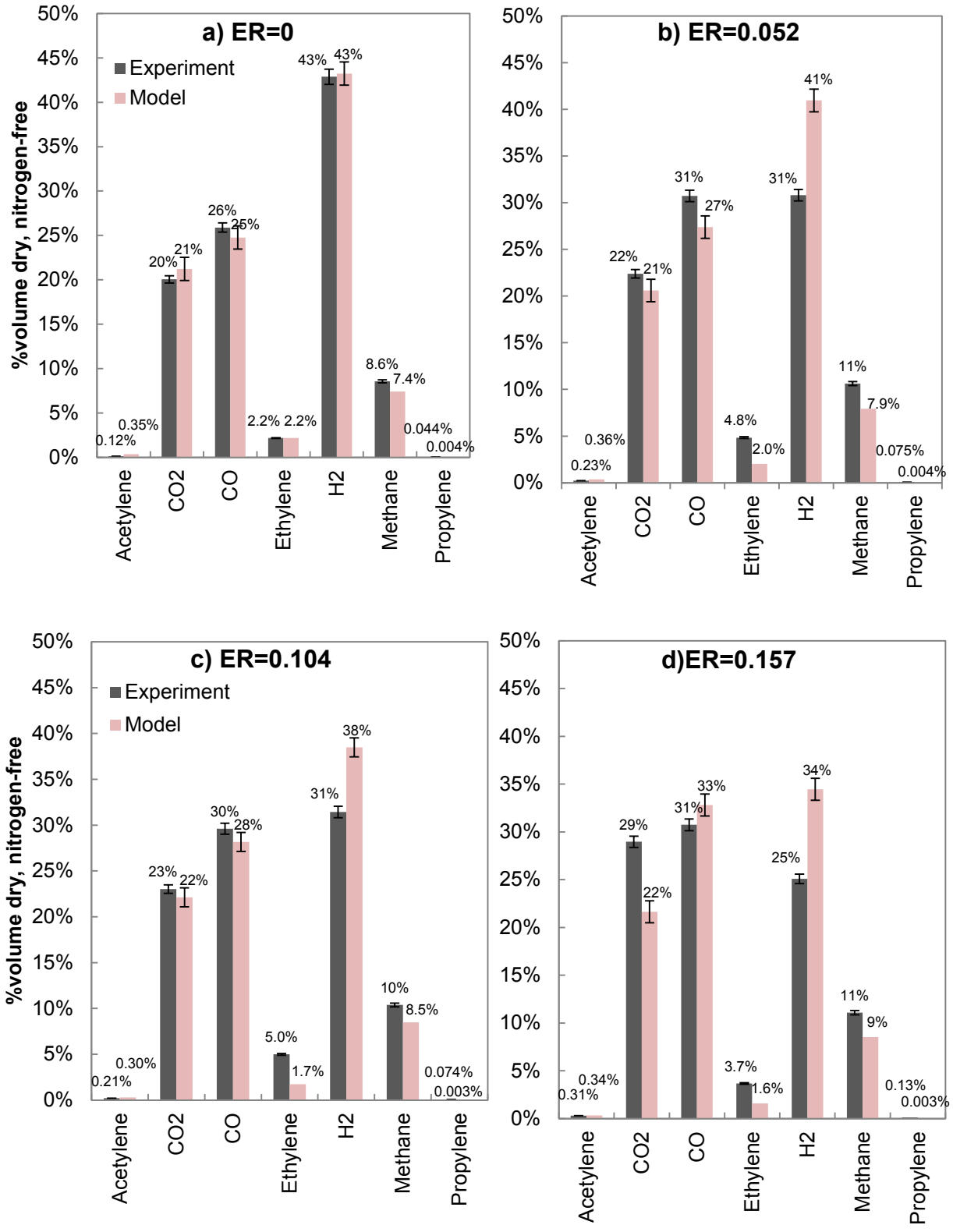

Figure 10 Concentration of major gas species (% dry, inert free) versus air fuel equivalence ratio ER=(0,0.052,0.104,0.157) for steam and air gasification of oak at 850°C

Hydrogen is shown to decrease as air is added in both the experiments (43-25%vol dry) and model predictions (43-34%vol dry, inert free). This can be partially explained by the lower steam injection rate which reduces the kinetics and driving potential for the forward WGSR. The experiments show that the CO_2 monotonically increases (from 20-28% vol.,dry) as more air is injected implying the oxidation of the carbon monoxide or methane. Meanwhile the CO_2 fraction from the model predictions are relatively stable around 21-22%vol,dry.

5.2.2. Tar species

Figure 11a,b show the influence of ER (ER= 0,0.052,0.104) on the concentration of tar species (% dry, inert free) for the experimental measurements and model predictions, respectively. MBMS data was not available for experiment #10 (ER=0.157).

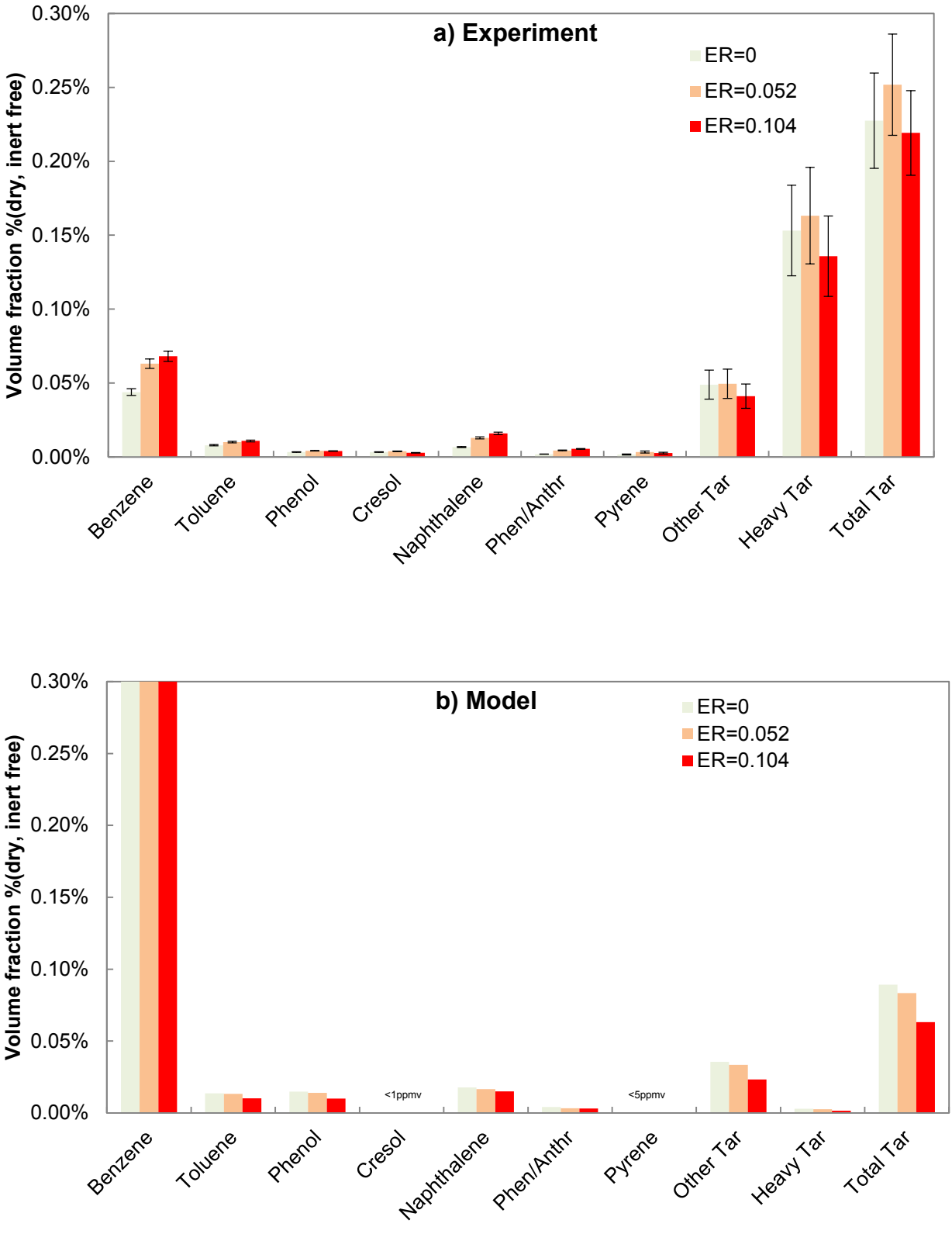

Figure 11 Concentration of tar species (% vol dry, inert free) versus air fuel equivalence ratio ER=(0,0.052,0.104) measured during experiments a) and predicted by model b) during steam and air gasification of oak at 850°C

Experimental results show an increase in “heavy” and total tar with an incremental amount of oxygen/air (ER=0.052). The former increases from 1500ppmv to 1600ppmv, and the latter from 2700ppmv to 3100ppmv. Additional air (ER=0.0104) appears to slightly decrease these quantities. Pyrene also displays a similar non-monotonic trend (17, 30, 27ppmv). Meanwhile the model predicts these categories as decreasing monotonically with additional oxygen. The model underpredicts “heavy” tar (15-30ppmv) by three orders of magnitude and cresol (<1ppmv) by an order of magnitude. Experimentally, benzene, naphthalene, and phenanthrene/anthracene are shown to monotonically increase with additional oxygen. For example, the experimentally measured naphthalene increases from 68ppmv to 159ppmv whereas the model predicts a slightly decreasing trend from 178ppm to 150ppm. Benzene is over-predicted by the model and comprises the majority of the predicted tar components. Both model and experiment demonstrate a decrease in “other” tars with additional air. The experimental concentrations of toluene and phenol appear relatively stable whereas the model actually predicts them decreasing by up to 50% with added oxygen/air.

Several reasons may explain why the model under-predicts heavy tars and over-predicts benzene. The first is related to the gas phase mixing assumptions. The growth of PAH’s is highly sensitive and non-linearly dependent on the local concentrations of oxygen, acetylene, and hydrogen radicals. Given the high rates of oxidation reactions, it is possible that oxygen and other radicals are not actually well mixed throughout the bed, creating locally-rich conditions that may accelerate ring formation and growth. Additionally, the largest molecule considered in the chemical kinetics mechanism is a lumped PAH called “BIN1B’ with a chemical formula of $C_{20}H_{16}$ (MW= 256.347 g/mol). Meanwhile the MBMS measures “heavy tars” with molecular weights up to 400 g/mol. It is possible a larger chemical kinetic mechanism may be required to

accurately describe the formation of these large soot-precursors. Lastly, the bed material, olivine, is known to reduce tar concentrations significantly through catalytic effects [114] which are not accounted for in the current chemical kinetic mechanism. More work is needed to develop detailed kinetic mechanisms which incorporate catalytic effects from the bed/ash material. Additionally, future efforts will consider incorporating more detailed solids/fuel mixing [115] and gas phase hydrodynamics to the CRNM.

Overall, the experimental results demonstrate that the introduction of oxygen may accelerate the conversion of smaller PAH's into higher molecular weight compounds. Instead of destroying tars, the oxygen appears to shift the composition of the tars from lighter PAH's to heavier ones.

5.2.3. Char conversion and inventory

In order to understand the impact of air injection on the overall gasifier performance, it is important to consider how char conversion is influenced by this variation. Figure 12a,b show the carbon elutriation rate and steady state carbon inventory versus ER, respectively for the oak gasification at 850°C.

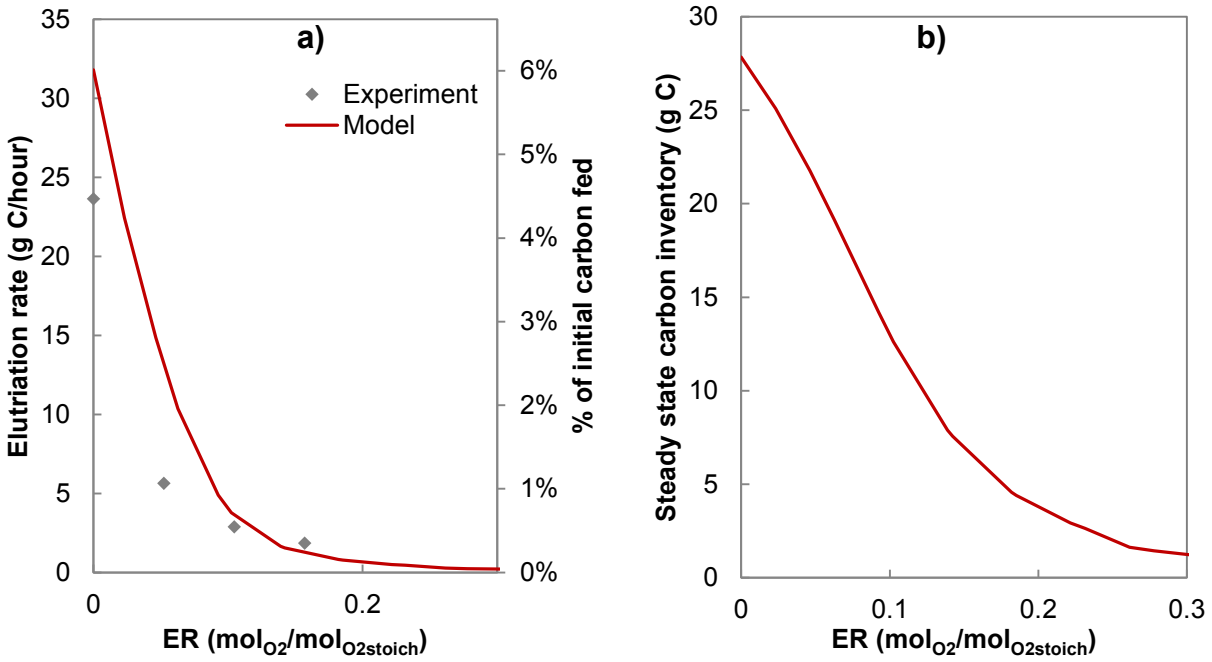

Figure 12 a) Char elutriation rate (gC/hour) and b) steady state carbon inventory (gC) versus ER (ER=0,0.052,0.104,0.157) for steam air gasification of oak at T=850°C

The experiments show that the introduction of oxygen drastically reduces the elutriation rate of carbon. 4-5% of the initial carbon contained in the biomass is initially blown out of the reactor when no air is injected. By increasing the ER to 0.157, this quantity is reduced to well below 1%- a significant improvement in the overall gasifier performance. Moreover, this quantitative agreement overcomes one of the major deficiencies in previous reactor models: many of which either neglected or over-predicted elutriation rates by orders of magnitude [91].

Another important conclusion is that a significant fraction of the additional oxygen reacts with the char rather than the light gas components. In fact the model shows that at an ER=0.052 70% of the oxygen reacts with the char. At ER=0.0154, this goes down to 53%, demonstrating that additional oxygen begins to combust the gas phase components.

The char inventory also decreases rapidly with the addition of oxygen from 27 grams (ER=0) to ~<3 grams (ER=0.157). In order to measure the steady state char inventory burnout, experiments were performed after steady operation was achieved. However, they were only done for select experiments. Nevertheless, the model predictions are well within the experimentally observed range which was less than 50g of carbon. This reduction in char inventory might also have significant solids mixing benefits, since excessive quantities of char build up may cause unwanted segregation and or ash agglomeration issues. Properties of the elutriated char/ash particles are summarized in Appendix 3.

5.2.4. Gasifier performance and efficiency

Figure 13a demonstrates the impact of ER on key gasifier metrics including the cold gas efficiency, η_{HHV}, char conversion (%wt initial char). Predicted char conversion (which includes conversion due to the release of trapped gases) is shown by the dotted line in Figure 13a, and it is

87% when no air is injected. At an ER=0.052 this increases rapidly to 95% conversion, which brings about an increase in the cold gas efficiency of the gasifier. The CGE is maximized (102% HHV) at this level of air injection. Additional air injection beyond this point helps to improve char conversion which is essentially complete beyond ER>0.157. Further increases in air injection oxidize the gasification products themselves reducing the CGE drastically.

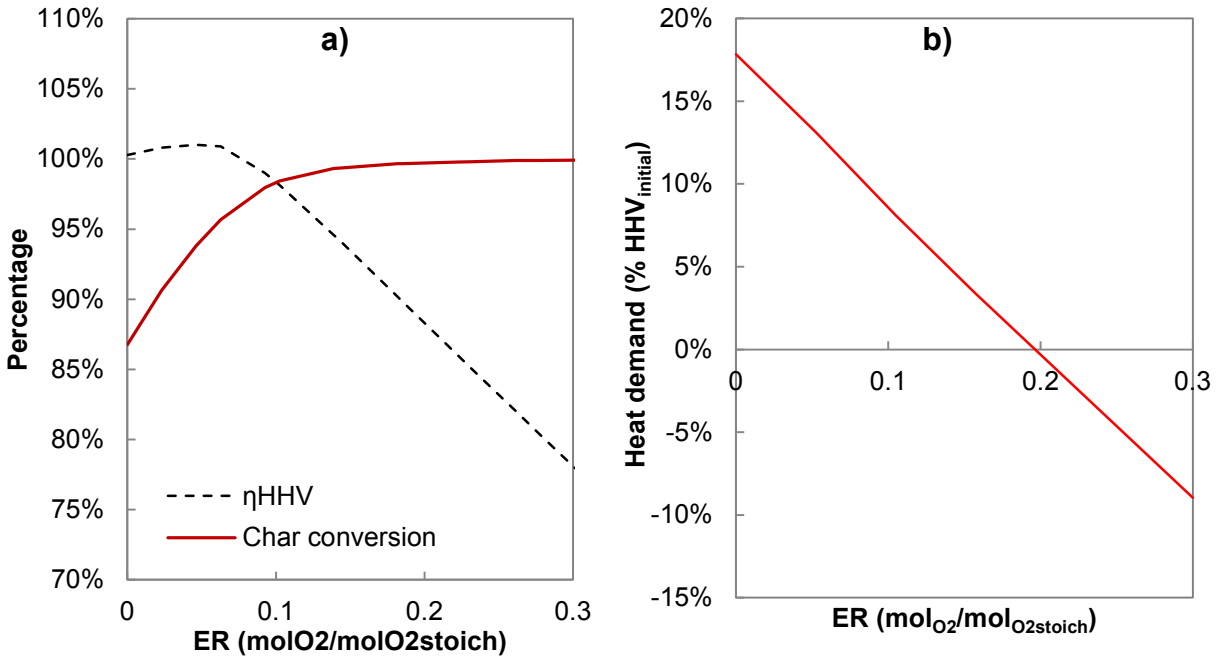

Figure 13 Char conversion (%wt initial char) a) and cold gas efficiency (%HHV) and net heat demand b) versus ER

The net heat demand versus ER shown in Figure 13b explains how it is possible for the CGE to be greater than 1. Since the net heat demand is positive the system is highly endothermic requiring energy to sustain the reaction temperature. In this case, the net heat required comes from the electrical heating wrapped around the reactor- which also acts to supply energy for heat losses to the environment.

At an ER of 0.2 and SBR of 0.6 the gasifier would be expected to achieve autothermal conditions: the sum of the heat generated/absorbed by the reactions is thermally neutral. Note that the heat demand for this gasifier (under practical operating conditions) would actually be significantly higher (and the efficiency lower) than shown above for two reasons: i) in the experiment, the incoming air/steam were pre-heated to the reaction temperature. Practically sized heat recovery systems would not be able to reach such a high temperatures ii) the reactor was externally heated so as to make up for any heat losses to the environment. The actual gasifier would experience significant heat losses [116], unless the diameter is very large and the reactor is well insulated.

In summary, this modeling study has identified, four possible ways to maximize the performance of the gasifier which each require different levels of air/steam injection, depending on the goal:

i) **Minimize heavy tar formation:** To avoid the formation of heavy PAH compounds, the gasifier should be operated with steam only, ER=0.

ii) **Maximize char conversion:** Char conversion increases monotonically with increasing ER, but beyond an ER of ~0.15 there appears to be little marginal benefit for the particle sizes in this study.

iii) **Maximize chemical efficiency**: CGE can be maximized at an ER~0.05, although the system is endothermic.

iv) **Minimize thermal input:** Autothermal operation is theoretically achievable at an ER=0.2 for an SBR=0.6 with fully pre-heated reactants.

Future work will consider a parametric study of these various operational parameters in order to find a set of operating conditions which can simultaneously achieve these performance goals.

6. Conclusion

The introduction of air into a steam blown fluidized bed gasifier has profound effects on its performance and outlet composition which have yet to be fully understood by previous modeling or experimental efforts because of the tremendous number of simultaneous physical and chemical phenomena. In this study, we have proposed and validated a coupled multi-scale modeling approach (CRNM) which accounts for the dominant processes including particle scale devolatilization, gas phase conversion, and char conversion. Appropriate values for sub-model parameters were taken from the literature or directly measured- they were not tuned or fitted in this study. Experiments were performed in a bench scale 4'' (10.16cm) fluidized bed steam/air blown gasifier using oak and hardwood sawdust feedstocks. Temperature and air/fuel equivalence ratio (ER) were varied in a parametric fashion in order to isolate their effects. Good agreement between the model predictions for the major gas, tar species, and elutriated char quantities was achieved across the range of experimental conditions. The experimental results show that the composition of tar is highly sensitive to the addition of oxygen, which appears to accelerate the conversion of lighter PAH's into soot precursors at a fixed operating temperature.

The model tends to over-predict the production of benzene and under-predict the rate of formation of heavy tar compounds. Experimental data and modeling results agree that the char reacts with very significant fraction of the added air, improving its overall conversion drastically and reducing the steady state bed inventory of char. Using the model, it was possible to identify conditions which maximized chemical efficiency- additional air injection beyond this point oxidizes the desirable gasification products.

Appendix 1 Calculation of reactor network model volumes

As shown in the Figure 4, the total internal volume of the reactor is defined by the bed diameter and height (d_{bed},H_{bed},) the freeboard diameter and height d_{fb} H_{fb} (freeboard diameter). The total volume of the two reactors must sum to this.

$$V_{tot} = \frac{\pi}{4}\left(d_{fb}^2 H_{fb} + d_{bed}^2 H_{bed}\right) = V_{CSTR} + V_{PFR} \tag{24}$$

The static bed height is computed based on the mass of bed material

$$H_s = \frac{m_b}{\rho_p A_c}\frac{1}{(1-\varepsilon_m)} \tag{25}$$

Where ε_m is the static packing void fraction and is 0.4 for most materials, and A_c is the cross sectional area of the bed. The height of the bed at minimum fluidizing conditions can be computed,

$$H_{mf} = \frac{m_b}{\rho_p A_c}\frac{1}{\left(1-\varepsilon_{mf}\right)} \tag{26}$$

Where the voidage at minimum fluidization depends on the sphericity Ψ,

$$\varepsilon_{mf} = \left(\frac{1}{14\Psi}\right)^{1/3} \tag{27}$$

Once the flow is increased beyond the minimum fluidizing velocity, u_{mf}, the bed expands further due to the presence of voids (i.e. bubbles). Because of the dependence of bed properties on height, the expansion must be estimated using an iterative method Zhu et al. [73] Firstly guess a value of $\bar{\delta}_i$,the fraction of dense bed volume occupied by bubbles. Then an initial estimate of the expanded bed depth is calculated,

$$H_i = \frac{H_{mf}}{1 - \bar{\delta}_i} \tag{28}$$

According to the two-phase theory of fluidization all flow in excess of minimum fluidization (u_0-u_{mf}) occurs through the bubble phase. Therefore, the bubble fraction can be computed from the average bubble velocity u_b, superficial gas velocity u_0, and minimum fluidizing velocity,

$$\delta = \frac{\dot{V}_b}{u_b A} = \frac{u_0 - u_{mf}}{u_b} \tag{29}$$

Next, the mean bubble diameter d_b and bubble rise velocity u_b can be evaluated at $z_i = \frac{H_i}{2}$ using the correlations in Table 5. The bubble rise velocity can be substituted into equation (29) resulting in a new estimate of bubble fraction δ_{i+1} and bed height H_{i+1}. After multiple iterations the estimated bed height reaches a steady value, $H_{i+1} \rightarrow H_{ex}$, and the volume of the bed region can be computed,

$$V_{CSTR} = H_{ex} d_{bed} \tag{30}$$

where the average gas volume fraction of the CSTR region is given by,

$$\varepsilon_{CSTR} = \delta \varepsilon_b + (1 - \delta)\varepsilon_{mf} \tag{31}$$

and the bubble void fraction, ε_b, is assumed to be 1. The solids volume fraction in the freeboard is assumed to be negligible ($\varepsilon_{PFR} = 1$) and based on the previously defined volume constraint in equation (24) , its volume can be computed.

$$V_{PFR} = V_{PFR} - V_{CSTR} \tag{32}$$

Table 5 Hydrodynamic correlations for estimation fluidized bed reactor network volumes

Quantity	Correlation	Source
Minimum fluidizing velocity, u_{mf} (m/s)	$\frac{\rho_f u_{mf} d_p}{\mu_f} = [33.7^2 + 0.0408Ar]^{0.5} - 33.7$	Wen and Yu, 1966 [117]
Bubble diameter, d_b (m)	$\frac{d_{b,m} - d_b}{d_{b,m} - d_{b,0}} = e^{-0.3z/d_{bed}}$	Mori and Wen, 1975 [118]
Initial bubble size, $d_{b,0}$ (m)	$d_{b,0} = \frac{3.69}{g}(u_0 - u_{mf})^2$	Mori and Wen, 1975 [118]
Maximum bubble diameter, $d_{b,m}$(m)	$d_{b,m} = \frac{2.59}{g^{0.2}}\left[\frac{\pi}{4} d_t^2 (u_0 - u_{mf})\right]^{0.4}$	Horio and Nonaka, 1987 [119]
Bubble rise velocity u_{br} (m/s)	$u_{br} = 0.711\sqrt{g d_b}$	Davidson and Harrison, 1963 [120]
Average bubble velocity u_b (m/s)	$u_b = u_0 - u_{mf} + u_{br}$	Davidson and Harrison, 1963 [120]

Appendix 2 Tar characterization

Table 6 Tars characterized by MBMS

	Structure	Formula	Molecular weight (g/mol)	Higher heating value (kJ/mol)
Benzene		C_6H_6	78.11	3,291.7
Toluene	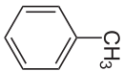	C_7H_8	92.14	3,934.8
Phenol	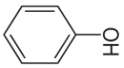	C_6H_5OH	94.11	3,112.3
Cresol	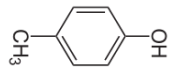	C_7H_8O	108.14	3,756.0
Naphthalene	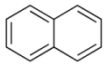	$C_{10}H_8$	128.17	5,216.0
Anthracene, Phenanthrene	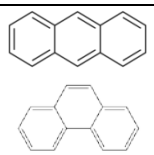	$C_{14}H_{10}$	178.23	7,131.0
Pyrene	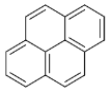	$C_{16}H_{10}$	202.25	7,939.8
Other tars			(129<MW<201)	
Heavy tars			(203<MW<400)	
Note: (not all isomers shown)				

Appendix 3 Elutriated char characterization

Proximate, ultimate, particle size distribution analyses of the elutriated chars during oak gasification experiments were performed and are summarized in Table 7. Samples were all taken from the first char pot which is directly downstream of the freeboard of the gasifier.

Table 7 Proximate and ultimate analysis of elutriated chars during air/steam gasification of oak.

Temperature	Feedstock	ER	Moisture	Ash	Volatile	Fixed Carbon	C	H	N	S	O (from chlorine)
°C		[]	(%wt)	(%wt)	(%wt)	(%wt)	(%wt,dry)	(%wt,dry)	(%wt,dry)	(%wt,dry)	(%wt,dry)
850	Oak	0	2.38	26.53	9.66	61.43	65.35	0.61	0.19	0.002	6.67
850	Oak	0.052	2.3	30.55	10.6	56.55	63.08	0.52	0.04	0.004	5.09
850	Oak	0.104	1.94	25.68	13.47	58.91	66.77	0.78	0.1	0.008	6.16
850	Oak	0.15	2.09	34.06	16.57	47.28	57.91	0.71	0.09	0.004	6.5

Elutriated char is primarily of carbon (47-60%wt), ash (~25-35%wt) and some volatiles (10-16%wt). On an ash-free basis, the char particles are >95% carbon. The char particles were log-normally distributed (with a Gaussian function) as shown in Figure 14. The ER=0.05 particle distribution is uni-modal at 41 microns while the oxygen free conditions (ER=0) resulted in a bi-modal distribution having a slightly larger mean particle diameter of 65 microns.

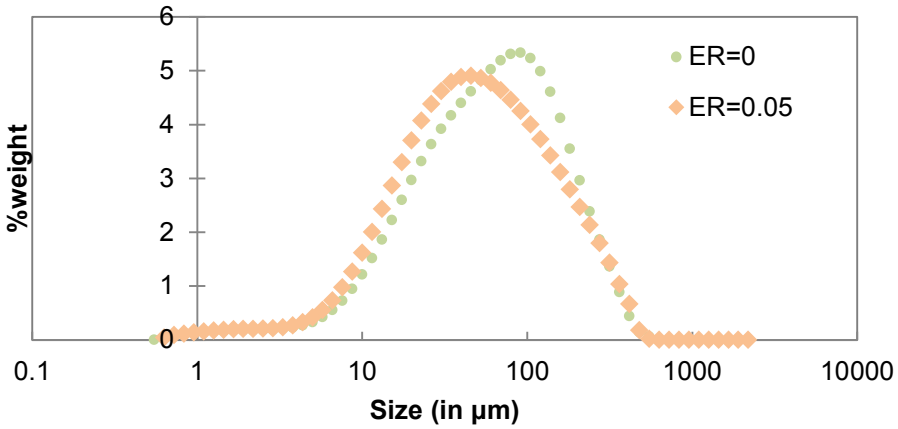

Figure 14 Particle size distribution (%wt versus µm) of elutriated char particles during oak air-steam gasification at 850°C

Nomenclature			
Notation		*Greek letters*	
A_c	cross sectional area (m^2)	δ	bubble fraction (m^3/m^3)
C	concentration ($kmol/m^3/s$ or $mol/m^3/s$)	ε_j	volume fraction ($m^3_j/m^3_{particle}$)
c_p	specific heat capacity (J/kg/K)	η	efficiency
d_p	particle volume/surface mean diameter (m)	μ_f	dynamic viscosity (Pa-s)
D	diffusivity (m^2/s)	ρ	density (kg/m^3)
F	molar flow rate (mol/sec)	τ	residence time or time-scale (sec)
g	gravitational acceleration (m/s^2)	φ_s	shrinkage factor ($m^3_{biomass}/m^3_{char}$)
H	height (m)	ψ	reactivity factor
h_i	Specific enthalpy (J/kg)	Ψ	sphericity
h_j	heat transfer coefficient (W/m^2K)	$\dot{\omega}$	net production rate ($mol/m^3/s$)
h_m	mass transfer coefficient (m/s)		
k	conductivity (W/mK)	*Subscripts*	
K	attrition constant	*att*	attrition
m	mass (kg)	*b*	bulk, bubble
MW	Molar mass ($kg\ mol^{-1}$)	*bio*	biomass
n_1	primary fragmentation factor	*c*	carbon
u_0	superficial gas velocity (m/s)	*ch*	char
P	Pressure (Pa)	*f*	fluid
Q	volumetric flow rate (m^3/s)	*fb*	freeboard
$\dot{Q}$	heat input/output (W)	*L*	lateral
q	structural attrition constant (-)	*s*	solid
R	reaction rate ($kmol/m^3/s$)	*wgs*	water gas shift
R_g	ideal gas constant (J/K/mol)		
t	time, time-scale (s)		
T	temperature (K)		
V	volume (m^3)		
X	mole fraction (mol/mol)		

Acknowledgements: The authors gratefully acknowledge BP for funding this research. Research facilities at the National Renewable Energy Laboratory are supported by the Bioenergy Technology Office and U.S. Department of Energy under contract number DE-AC36-08-GO28308. This research was supported in part by an appointment to the National Energy Technology Laboratory Research Participation Program, sponsored by the U.S. Department of Energy and administered by the Oak Ridge Institute for Science and Education. This contribution was identified by Michael Molnar (Hemlock Semiconductor Group) as the Best Presentation in the session "Fluidization and Fluid-Particle Systems for Energy and Environmental Applications" of the 2015 AIChE Annual Meeting in Salt Lake City.

ABBREVIATIONS

FBBG, fluidized bed biomass gasification; BFB bubbling fluidized bed; BTL biomass to liquids, ER air-fuel equivalence ratio, MBMS molecular beam mass spectrometer, NEHW New England hardwood, polycyclic aromatic hydrocarbons (PAH), SBR steam to biomass ratio, WGSR water gas shift reaction,

List of Figure Captions

Figure 1 Particle and reactor scale processes occurring during fluidized bed gasification

Figure 2 Time scales for particle devolatilization and mixing versus biomass particle diameter (in mm)

Figure 3 Time scale (seconds) of homogeneous and heterogeneous reactions during fluidized bed gasification versus temperature ($^{\circ}$C)

Figure 4 Reactor network geometry derived from actual geometry

Figure 5 Couple reactor network model (CRNM) solution algorithm

Figure 6 Schematic of 4inch bench scale steam/air blown gasification reactor, sampling, collection, and characterization equipment A, pneumatic screw feeding system, B- fluidization agent preheating system C- gasifier D solids capture system E-scrubber system, F- gas filtration and sampling system

Figure 7 Concentration of major gas species (%vol. inert free) versus bed temperature during steam gasification. a-c) corresponds to NEWH, (d-f) corresponds to oak at bed temperatures of 750,800,850°C, respectively.

Figure 8 Water gas shift equilibrium coefficient Kwgsr [-] versus bed temperature in $^{\circ}$C.

Figure 9 Concentration of tar species (%wet, inert free) versus temperature measured during experiments a) and predicted by model b) under steam-blown oak gasification conditions.

Figure 10 Concentration of major gas species (% dry, inert free) versus air fuel equivalence ratio ER=(0,0.052,0.104,0.157) for steam and air gasification of oak at 850$^{\circ C}$

Figure 11 Concentration of tar species (% vol dry, inert free) versus air fuel equivalence ratio ER=(0,0.052,0.104) measured during experiments a) and predicted by model b) during steam and air gasification of oak at 850$^{\circ C}$

Figure 12 a) Char elutriation rate (gC/hour) and b) steady state carbon inventory (gC) versus ER (ER=0,0.052,0.104,0.157) for steam air gasification of oak at T=850$^{\circ C}$

Figure 13 Char conversion (%wt initial char) a) and cold gas efficiency (%HHV) and net heat demand b) versus ER

Figure 14 Particle size distribution (%wt versus μm) of elutriated char particles during oak air-steam gasification at 850°C

Literature Cited

1. UNFCCC. *Paris Agreement*. (2015).
2. U.S. Department of Energy. *U.S. Billion ton update: Biomass supply for a bioenergy and bioproducts industry*. 227 (Oak Ridge National Laboratory, 2011).
3. Carpenter, D., Westover, T. L., Czernik, S. & Jablonski, W. Biomass feedstocks for renewable fuel production: a review of the impacts of feedstock and pretreatment on the yield and product distribution of fast pyrolysis bio-oils and vapors. *Green Chem.* **16,** 384–406 (2014).
4. Higman, C. & van der Burgt, M. *Gasification*. (Gulf Professional Printing, 2003).
5. Reed, C. L. & Kuhre, C. J. in *Hydrogen: Production and Marketing* **116,** 95–121 (American Chemical Society, 1980).
6. Hofbauer, H. *et al.* in *Developments in Thermochemical Biomass Conversion* (eds. Bridgwater, A. V. & D.G.B. Boocock) 1016–1025 (Blackie Academic & Professional, 1997).
7. Heidenreich, S. & Foscolo, P. U. New concepts in biomass gasification. *Prog. Energy Combust. Sci.* **46,** 72–95 (2015).
8. Campoy, M., Gómez-Barea, A., Vidal, F. B. & Ollero, P. Air–steam gasification of biomass in a fluidised bed: Process optimisation by enriched air. *Fuel Process. Technol.* **90,** 677–685 (2009).
9. Narváez, I., Orío, A., Aznar, M. P. & Corella, J. Biomass Gasification with Air in an Atmospheric Bubbling Fluidized Bed. Effect of Six Operational Variables on the Quality of the Produced Raw Gas. *Ind Eng Chem Res* **35,** 2110–2120 (1996).

10. Göransson, K., Söderlind, U., He, J. & Zhang, W. Review of syngas production via biomass DFBGs. *Renew. Sustain. Energy Rev.* **15,** 482–492 (2011).

11. Corella, J., Toledo, J. M. & Molina, G. Calculation of the conditions to get less than 2 g tar/mn3 in a fluidized bed biomass gasifier. *Fuel Process. Technol.* **87,** 841–846 (2006).

12. Chembukulam, S. K., Dandge, A. S., Rao, N. L. K., Seshagiri, K. & Vaidyeswaran, R. Smokeless fuel from carbonized sawdust. *Ind. Eng. Chem. Prod. Res. Dev.* **20,** 714–719 (1981).

13. Milne, T. ., Evans, R. J. & Abatzoglou, N. *Biomass gasifier 'tars': Their nature, formation and conversion*. (National Energy Technology Laboratory (NETL), 1998).

14. Bates, R. B., Altantzis, C. & Ghoniem, A. F. Modeling of Biomass Char Gasification, Combustion, and Attrition Kinetics in Fluidized Beds. *Energy Fuels* **30,** 360–376 (2016).

15. Bayarsaikhan, B. *et al.* Inhibition of steam gasification of char by volatiles in a fluidized bed under continuous feeding of a brown coal. *Fuel* **85,** 340–349 (2006).

16. H. Thunman & Seemann, M. C. First experiences with the new Chalmers gasifier. in *Proceedings of the 20th International Conference on Fluidized bed Combustion* 659–663 (Springer-Verlag, 2010).

17. Campoy, M., Gómez-Barea, A., Villanueva, A. L. & Ollero, P. Air−Steam Gasification of Biomass in a Fluidized Bed under Simulated Autothermal and Adiabatic Conditions. *Ind. Eng. Chem. Res.* **47,** 5957–5965 (2008).

18. R.J. Evans, Knight, R. A., Onischak, M. & Babu, S. P. *Development of biomass gasification to produce substitute fuels*. (Pacific Northwest National Lab, 1988).

19. Guéret, C., Daroux, M. & Billaud, F. Methane pyrolysis: thermodynamics. *Chem. Eng. Sci.* **52,** 815–827 (1997).

20. Sauciuc, A., Dumitrescu, L., Manciulea, I., Rauch, R. & Hofbauer, H. in *Sustainable Energy in the Built Environment - Steps Towards nZEB* (ed. Visa, I.) 335–346 (Springer International Publishing, 2014).

21. Kiel, J. H. A. *et al. Primary measure to reduce tar formation in fluidised-bed biomass gasifiers*. (Energy Research Center of the Netherlands, 2004).

22. Valin, S., Ravel, S., Guillaudeau, J. & Thiery, S. Comprehensive study of the influence of total pressure on products yields in fluidized bed gasification of wood sawdust. *Fuel Process. Technol.* **91,** 1222–1228 (2010).

23. Corella, J., Toledo, J. M. & Padilla, R. Olivine or Dolomite as In-Bed Additive in Biomass Gasification with Air in a Fluidized Bed: Which Is Better? *Energy Fuels* **18,** 713–720 (2004).

24. Franco, C., Pinto, F., Gulyurtlu, I. & Cabrita, I. The study of reactions influencing the biomass steam gasification process. *Fuel* **82,** 835–842 (2003).

25. Gómez-Barea, A., Ollero, P. & Leckner, B. Optimization of char and tar conversion in fluidized bed biomass gasifiers. *Fuel* **103,** 42–52 (2013).

26. Gómez-Barea, A. & Leckner, B. Estimation of gas composition and char conversion in a fluidized bed biomass gasifier. *Fuel* **107,** 419–431 (2013).

27. Weimer, A. W. & Clough, D. E. Modeling a low pressure steam-oxygen fluidized bed coal gasifying reactor. *Chem. Eng. Sci.* **36,** 548–567 (1981).

28. Pan, Y. ., Roca, X., Velo, E. & Puigjaner, L. Removal of tar by secondary air in fluidised bed gasification of residual biomass and coal. *Fuel* **78,** 1703–1709 (1999).

29. Campoy, M., Gómez-Barea, A., Fuentes-Cano, D. & Ollero, P. Tar Reduction by Primary Measures in an Autothermal Air-Blown Fluidized Bed Biomass Gasifier. *Ind. Eng. Chem. Res.* **49,** 11294–11301 (2010).

30. Lv, P. . *et al.* An experimental study on biomass air–steam gasification in a fluidized bed. *Bioresour. Technol.* **95,** 95–101 (2004).

31. Koppatz, S., Pfeifer, C. & Hofbauer, H. Comparison of the performance behaviour of silica sand and olivine in a dual fluidised bed reactor system for steam gasification of biomass at pilot plant scale. *Chem. Eng. J.* **175,** 468–483 (2011).

32. Rauch, R. *et al.* Steam Gasification of Biomass at CHP Plant in Guessing - Status of the Demonstration Plant. in (2004).

33. Carpenter, D. L. *et al.* Pilot-Scale Gasification of Corn Stover, Switchgrass, Wheat Straw, and Wood: 1. Parametric Study and Comparison with Literature. *Ind Eng Chem Res* **49,** 1859–1871 (2010).

34. Schuetzle, D., Schuetzle, R., Kent Hoekman, S. & Zielinska, B. The effect of oxygen on formation of syngas contaminants during the thermochemical conversion of biomass. *Int. J. Energy Environ. Eng.* **6,** 405–417 (2015).

35. Henriksen, U. *et al.* The design, construction and operation of a 75 kW two-stage gasifier. *ECOS 2003* **31,** 1542–1553 (2006).

36. Nilsson, S., Gómez-Barea, A., Fuentes-Cano, D. & Ollero, P. Gasification of biomass and waste in a staged fluidized bed gasifier: Modeling and comparison with one-stage units. *Fuel* **97,** 730–740 (2012).

37. Hayashi, J. *et al.* Low-Temperature Gasification of Biomass and Lignite: Consideration of Key Thermochemical Phenomena, Rearrangement of Reactions, and Reactor Configuration. *Energy Fuels* **28,** 4–21 (2013).

38. Kunii, D. & Levenspiel, O. *Fluidization engineering*. (Butterworth-Heinemann, 1991).

39. Rowe, P. N. & Partridge, B. A. Particle movement caused by bubbles in a fluidized bed. *Proc. Symp. Interact. Fluids Part. Inst Chem Engrs* 135 (1962).

40. Petersen, I. & Werther, J. Three-dimensional modeling of a circulating fluidized bed gasifier for sewage sludge. *Chem. Eng. Sci.* **60,** 4469–4484 (2005).

41. Bilbao, R., Lezaun, J., Menéndez, M. & Abanades, J. C. Model of mixing—segregation for straw/sand mixtures in fluidized beds. *Powder Technol.* **56,** 149–155 (1988).

42. Lin, L., Sears, J. T. & Wen, C. Y. Elutriation and attrition of char from a large fluidized bed. *Powder Technol.* **27,** 105–115 (1980).

43. Bartels, M., Lin, W., Nijenhuis, J., Kapteijn, F. & van Ommen, J. R. Agglomeration in fluidized beds at high temperatures: Mechanisms, detection and prevention. *Prog. Energy Combust. Sci.* **34,** 633–666 (2008).

44. Neves, D., Thunman, H., Matos, A., Tarelho, L. & Gomez-Barea, A. Characterization and prediction of biomass pyrolysis products. *Prog. Energy Combust. Sci.* **37,** 611–630 (2011).

45. Gomez-Barea, A. & Leckner, B. Modeling of biomass gasification in fluidized bed. *Prog. Energy Combust. Sci.* **36,** 444–509 (2010).

46. Corella, J., Toledo, J. M. & Aznar, M.-P. Improving the Modeling of the Kinetics of the Catalytic Tar Elimination in Biomass Gasification. *Ind. Eng. Chem. Res.* **41,** 3351–3356 (2002).

47. Bruni, G. *et al.* Self-segregation of high-volatile fuel particles during devolatilization in a fluidized bed reactor. *Powder Technol.* **128,** 11–21 (2002).

48. Yan, H., Heidenreich, C. & Zhang, D. Mathematical modelling of a bubbling fluidised-bed coal gasifier and the significance of 'net flow'. *Fuel* **77,** 1067–1079 (1998).

49. Ammendola, P., Chirone, R., Miccio, F., Ruoppolo, G. & Scala, F. Devolatilization and Attrition Behavior of Fuel Pellets during Fluidized-Bed Gasification. *Energy Fuels* **25,** 1260–1266 (2011).

50. Gerber, S., Behrendt, F. & Oevermann, M. An Eulerian modeling approach of wood gasification in a bubbling fluidized bed reactor using char as bed material. *Fuel* **89,** 2903–2917 (2010).

51. Xie, J., Zhong, W., Jin, B., Shao, Y. & Huang, Y. Eulerian–Lagrangian method for three-dimensional simulation of fluidized bed coal gasification. *Adv. Powder Technol.* (2013). doi:10.1016/j.apt.2012.09.001

52. Xie, J., Zhong, W., Jin, B., Shao, Y. & Liu, H. Simulation on gasification of forestry residues in fluidized beds by Eulerian–Lagrangian approach. *Bioresour. Technol.* **121,** 36–46 (2012).

53. Raman, P., Walawender, W. P., Fan, L. T. & Chang, C. C. Mathematical model for the fluid-bed gasification of biomass materials. Application to feedlot manure. *Ind. Eng. Chem. Process Des. Dev.* **20,** 686–692 (1981).

54. Corella, J., Herguido, J., Toledo, J. M. & Gomez-Civicos, J. I. in *1st World Conference on Biomass for Energy and Industry* **2,** 1971–1975 (James & James (Sciente Publishers Ltd)., 2001).

55. Kaushal, P. & Abedi, J. A simplified model for biomass pyrolysis in a fluidized bed reactor. *J. Ind. Eng. Chem.* **16,** 748–755 (2010).

56. Srinivas, S., Field, R. P. & Herzog, H. J. Modeling Tar Handling Options in Biomass Gasification. *Energy Fuels* **27,** 2859–2873 (2013).

57. Fuentes-Cano, D., Gómez-Barea, A., Nilsson, S. & Ollero, P. Kinetic modeling of tar and light hydrocarbons during the thermal conversion of biomass. *Energy Fuels* (2015). doi:10.1021/acs.energyfuels.5b02131

58. Stark, A. K., Bates, R. B., Zhao, Z. & Ghoniem, A. F. Prediction and Validation of Major Gas and Tar Species from a Reactor Network Model of Air-Blown Fluidized Bed Biomass Gasification. *Energy Fuels* **29,** 2437–2452 (2015).

59. Ranzi, E., Corbetta, M., Manenti, F. & Pierucci, S. Kinetic modeling of the thermal degradation and combustion of biomass. *Chem. Eng. Sci.* **110,** 2–12 (2014).

60. Norinaga, K. *et al.* A mechanistic study on the reaction pathways leading to benzene and naphthalene in cellulose vapor phase cracking. *Biomass Bioenergy* **69,** 144–154 (2014).

61. Yang, H.-M., Appari, S., Kudo, S., Hayashi, J. & Norinaga, K. Detailed Chemical Kinetic Modeling of Vapor-Phase Reactions of Volatiles Derived from Fast Pyrolysis of Lignin. *Ind. Eng. Chem. Res.* **54,** 6855–6864 (2015).

62. Nikoo, M. B. & Mahinpey, N. Simulation of biomass gasification in fluidized bed reactor using ASPEN PLUS. *Biomass Bioenergy* **32,** 1245–1254 (2008).

63. Radmanesh, R., Chaouki, J. & Guy, C. Biomass gasification in a bubbling fluidized bed reactor: Experiments and modeling. *AIChE J.* **52,** 4258–4272 (2006).

64. Bilodeau, J.-F., Thérien, N., Proulx, P., Czernik, S. & Chornet, E. A mathematical model of fluidized bed biomass gasification. *Can. J. Chem. Eng.* **71,** 549–557 (1993).

65. Corella, J. & Sanz, A. Modeling circulating fluidized bed biomass gasifiers. A pseudo-rigorous model for stationary state. *Fuel Process. Technol.* **86,** 1021–1053 (2005).

66. Jiang, H. & Morey, R. V. A numerical model of a fluidized bed biomass gasifier. *Biomass Bioenergy* **3,** 431–447 (1992).

67. Liu, H. & Gibbs, B. M. Modeling NH3 and HCN emissions from biomass circulating fluidized bed gasifiers☆. *Fuel* **82,** 1591–1604 (2003).

68. Sadaka, S. S., Ghaly, A. . & Sabbah, M. . Two phase biomass air-steam gasification model for fluidized bed reactors: Part II—model sensitivity. *Biomass Bioenergy* **22,** 463–477 (2002).

69. Souza-Santos, M. L. D. Application of comprehensive simulation of fluidized bed reactors to the pressurized gasification of biomass. *J. Braz. Soc. Mech. Sci.* **16,** 376–383 (1994).

70. Hamel, S. & Krumm, W. Mathematical modeling and simulation of bubbling fluidized bed gasifiers. *Fuel Energy Abstr.* **43,** 249 (2002).

71. Dupont, C., Boissonnet, G., Seiler, J.-M., Gauthier, P. & Schweich, D. Study about the kinetic processes of biomass steam gasification. *Fuel* **86,** 32–40 (2007).

72. Gomez-Barea, A., Nilsson, S., Vidal Barrero, F. & Campoy, M. Devolatilization of wood and wastes in fluidized bed. *Fuel Process. Technol.* **91,** 1624–1633 (2010).

73. Zhu, J., Bo Leckner, Yi Cheng & John Grace. in *Multiphase Flow Handbook* 5-1-5–93 (CRC Press, 2005).

74. Borodulya, V. A., Epanov, Y. G. & Teplitskii, Y. S. Horizontal particle mixing in a free fluidized bed. *J. Eng. Phys.* **42,** 528–533 (1982).

75. Gaston, K. R. *et al.* Biomass Pyrolysis and Gasification of Varying Particle Sizes in a Fluidized-Bed Reactor. *Energy Fuels* **25,** 3747–3757 (2011).

76. Biagini, E., Fantozzi, C. & Tognotti, L. Characterization of devolatilization of secondary fuels in different conditions. *Combust. Sci. Technol.* **176,** 685–703 (2004).

77. Decker, N. & Glicksman, L. R. Heat transfer in large particle fluidized beds. *Int. J. Heat Mass Transf.* **26,** 1307–1320 (1983).

78. Parker, W. J. *Development of a model for the heat release rate of wood: A status report*. 106 (US National Bureau of Standards, 1985).

79. Rowe, P. N. Estimation of solids circulation rate in a bubbling fluidised bed. *Chem. Eng. Sci.* **28,** 979–980 (1973).

80. Leckner, B. & Werther, J. Scale-up of Circulating Fluidized Bed Combustion. *Energy Fuels* **14,** 1286–1292 (2000).

81. Maku, T. Studies on the heat conduction in wood. *Kyoto Univ. Bull. Wood Res. Inst.* **13,** 1–80 (1954).

82. Grønli, M. G. A theoretical and experimental study of the thermal degradation of biomass. (Norwegian University of Science and Technology, 1996).

83. Baskakov, A. P. in *Fluidization* (ed. Davidson, J. F.) 465–471 (Academic Press, 1985).

84. Scala, F. & Salatino, P. Modelling fluidized bed combustion of high-volatile solid fuels. *Chem. Eng. Sci.* **57,** 1175–1196 (2002).

85. Marias, F., Puiggali, J. R. & Flamant, G. Effects of Freeboard Volatile Release During Fluidized Bed Incineration of a Model Waste. *Process Saf. Environ. Prot.* **79,** 244–252 (2001).

86. Agarwal, P. K. Transport phenomena in multi-particle systems—IV. Heat transfer to a large freely moving particle in gas fluidized bed of smaller particles. *Chem. Eng. Sci.* **46,** 1115–1127 (1991).

87. Olsson, J. Fuel dispersion and bubble flow distribution in fluidized beds. (Chalmers University of Technology, 2011).

88. Reschmeier, R. & Karl, J. Experimental study of wood char gasification kinetics in fluidized beds. *Biomass Bioenergy* **85,** 288–299 (2016).

89. Westbrook, C. . & Dryer, F. Simplified Reaction Mechanisms for the Oxidation of Hydrocarbon Fuels in Flames. *Combust. Sci. Technol.* **27,** 31–43 (1981).

90. Isaac, B. J. *et al.* A Novel Methodology for Chemical Time Scale Evaluation with Detailed Chemical Reaction Kinetics. *Energy Fuels* **27,** 2255–2265 (2013).

91. Souza-Santos, M. L. D. A new version of CSFB, comprehensive simulator for fluidised bed equipment. *Fuel* **86,** 1684–1709 (2007).

92. Marinov, N. M., Westbrook, C. K. & Pitz, W. J. in *Transport Phenomena in Combustion* 118–129 (Taylor & Francis, 1996).

93. Dryer, F. L. & Glassman, I. High-temperature oxidation of CO and CH4. *Fourteenth Symp. Int. Combust.* **14,** 987–1003 (1973).

94. Dufour, A. *et al.* Mechanisms and Kinetics of Methane Thermal Conversion in a Syngas. *Ind. Eng. Chem. Res.* **48,** 6564–6572 (2009).

95. Boroson, M. L., Howard, J. B., Longwell, J. P. & Peters, W. A. Product yields and kinetics from the vapor phase cracking of wood pyrolysis tars. *AIChE J.* **35,** 120–128 (1989).

96. Biba, V., Macak, J., Klose, E. & Malecha, J. Mathematical Model for the Gasification of Coal under Pressure. *Ind. Eng. Chem. Process Des. Dev.* **17,** 92–98 (1978).

97. Souza-Santos, M. L. de. *Solid fuels combustion and gasification : modeling, simulation, and equipment operation / Marcio L. de Souza-Santos.* (Marcel Dekker, 2004).

98. Di Blasi, C., Buonanno, F. & Branca, C. Reactivities of some biomass chars in air. *Carbon* **37,** 1227–1238 (1999).

99. van Paasen, S. V. B. & Kiel, J. H. A. *Tar formation in a fluidised bed gasifier*. (Energy Research Center of the Netherlands, 2004).

100. Wang, L., Liu, Z., Chen, S. & Zheng, C. Comparison of Different Global Combustion Mechanisms Under Hot and Diluted Oxidation Conditions. *Combust. Sci. Technol.* **184,** 259–276 (2012).

101. Di Blasi, C. Dynamic behaviour of stratified downdraft gasifiers. *Chem. Eng. Sci.* **55,** 2931–2944 (2000).

102. Vilienskii, T. V. & Hezmalian, D. M. Dynamics of the combustion of pulverized fuel. *Energiya* **11,** 246–251 (1978).

103. Jensen, A. *et al.* Formation and reduction of NOx in pressurized fluidized bed combustion of coal. *Fuel* **74,** 1555–1569 (1995).

104. Debiagi, P. E. A. *et al.* Extractives Extend the Applicability of Multistep Kinetic Scheme of Biomass Pyrolysis. *Energy Fuels* (2015). doi:10.1021/acs.energyfuels.5b01753

105. Bates, R. B. & Ghoniem, A. F. Modeling kinetics-transport interactions during biomass torrefaction: The effects of temperature, particle size, and moisture content. *Fuel* **137,** 216–229 (2014).

106. Turnbull, E. & Davidson, J. F. Fluidized combustion of char and volatiles from coal. *AIChE J.* **30,** 881–889 (1984).

107. Sridhar, R. Chemistry Models for Major Gas Species Estimation and Tar Prediction in Fluidized Bed Biomass Gasification. (Massachusetts Institute of Technology, 2016).

108. Abdelouahed, L. *et al.* Detailed Modeling of Biomass Gasification in Dual Fluidized Bed Reactors under Aspen Plus. *Energy Fuels* **26,** 3840–3855 (2012).

109. Goodwin, D. G., Moffat, H. K. & Speth, R. L. *Cantera: An object- oriented software toolkit for chemical kinetics, thermodynamics, and transport processes.* (2016).

110. Kee, R. J., Rupley, F., Meeks, E. & Miller, J. A. *CHEMKIN-III: A fortran chemical kinetics package for the analysis of gas phase chemical and plasma kinetics*. (Sandia National Laboratories, 1996).

111. Miller, R. S. & Bellan, J. *A generalized biomass pyrolysis model based on superimposed cellulose hemicellulose and lignin kinetics*. (NASA Jet Propulsion Laboratory, 1996).

112. Koufopanos, C. A., Papayannakos, N., Maschio, G. & Lucchesi, A. Modelling of the pyrolysis of biomass particles. Studies on kinetics, thermal and heat transfer effects. *Can. J. Chem. Eng.* **69,** 907–915 (1991).

113. Carpenter, D. L., Deutch, S. P. & French, R. J. Quantitative Measurement of Biomass Gasifier Tars Using a Molecular-Beam Mass Spectrometer: Comparison with Traditional Impinger Sampling. *Energy Fuels* **21,** 3036–3043 (2007).

114. Cheah, S. *et al.* Effects of thermal pretreatment and catalyst on biomass gasification efficiency and syngas composition. *Green Chem.* (2016). doi:10.1039/C6GC01661H

115. Stark, A. K., Altantzis, C., Bates, R. B. & Ghoniem, A. F. Towards an Advanced Reactor Network Modeling Framework for Fluidized Bed Biomass Gasification: Incorporating Information from Detailed CFD Simulations. *Chem. Eng. J.* **303,** 409–424 (2016).

116. Schoeters, J., Maniatis, K. & Buekens, A. Biomass Gasification (Part II) The fluidized-bed gasification of biomass: Experimental studies on a bench scale reactor. *Biomass* **19,** 129–143 (1989).

117. Wen, C. Y. & Yu, Y. H. A generalized method for predicting the minimum fluidization velocity. *AIChE J.* **12,** 610–612 (1966).

118. Mori, S. & Wen, C. Y. Estimation of bubble diameter in gaseous fluidized beds. *AIChE J.* **21,** 109–115 (1975).

119. Horio, M. & Nonaka, A. A generalized bubble diameter correlation for gas-solid fluidized beds. *AIChE J.* **33,** 1865–1872 (1987).

120. Davidson, J. . & Harrison, D. *Fluidised particles*. (Cambridge University Press, 1963).